IUPAC Technical Report

Roberto Terzano*, Melissa A. Denecke, Gerald Falkenberg, Bradley Miller, David Paterson and Koen Janssens

Recent advances in analysis of trace elements in environmental samples by X-ray based techniques (IUPAC Technical Report)

https://doi.org/10.1515/pac-2018-0605
Received June 21, 2018; accepted March 13, 2019

Abstract: Trace elements analysis is a fundamental challenge in environmental sciences. Scientists measure trace elements in environmental media in order to assess the quality and safety of ecosystems and to quantify the burden of anthropogenic pollution. Among the available analytical techniques, X-ray based methods are particularly powerful, as they can quantify trace elements *in situ*. Chemical extraction is not required, as is the case for many other analytical techniques. In the last few years, the potential for X-ray techniques to be applied in the environmental sciences has dramatically increased due to developments in laboratory instruments and synchrotron radiation facilities with improved sensitivity and spatial resolution. In this report, we summarize the principles of the X-ray based analytical techniques most frequently employed to study trace elements in environmental samples. We report on the most recent developments in laboratory and synchrotron techniques, as well as advances in instrumentation, with a special attention on X-ray sources, detectors, and optics. Lastly, we inform readers on recent applications of X-ray based analysis to different environmental matrices, such as soil, sediments, waters, wastes, living organisms, geological samples, and atmospheric particulate, and we report examples of sample preparation.

Keywords: environment; plants; sediments; soil; synchrotron; trace elements; wastes; XAS; XCMT; X-rays; XRD; XRF.

CONTENTS

Article note: Sponsoring body: IUPAC Chemistry and the Environment Division: see more details on page 1058.

***Corresponding author: Roberto Terzano,** Department of Soil, Plant and Food Sciences, University of Bari, Via Amendola 165/A, 70126 Bari, Italy, e-mail: roberto.terzano@uniba.it
Melissa A. Denecke: The University of Manchester, Dalton Nuclear Institute, Oxford Road, Manchester M14 9PL, UK
Gerald Falkenberg: Deutsches Elektronen-Synchrotron DESY, Photon Science, Notkestr. 85, 22603 Hamburg, Germany
Bradley Miller: United States Environmental Protection Agency, National Enforcement Investigations Center, Lakewood, Denver, CO 80225, USA
David Paterson: Australian Synchrotron, ANSTO Clayton Campus, Clayton, Victoria 3168, Australia
Koen Janssens: Department of Chemistry, University of Antwerp, Groenenborgerlaan 171, B-2020 Antwerp, Belgium

1 Introduction

X-ray based techniques for elemental analyses have advanced dramatically over the last two decades. The use of X-ray based techniques has expanded into a wide variety of scientific disciplines. These include the materials sciences, including metallurgy and mineralogy [1]; the environmental sciences, such as soil and water chemistry [2]; as well as the biological sciences [3–5]. The recent development and availability of X-ray based techniques, in particular those making use of synchrotron light sources, have significantly increased our understanding of the role of trace elements in the environment and in living organisms.

Trace elements, trace metal(loid)s, minor elements, and micronutrients are terms used in a number of sciences and the terms have some commonality. Historically, geologists considered trace elements to be "all elements except the eight abundant rock-forming elements: oxygen, silicon, aluminium, iron, calcium, sodium, potassium, and magnesium" [6]. Therefore, elements at concentrations of 0.1 % and lower were considered trace elements. The IUPAC Gold Book defines trace elements as "Any element having an average concentration of less than about 100 parts per million atoms" [7].

Trace elements in environmental matrices can be studied with a wide array of analytical techniques. These are usually selected based on the aggregation state of the sample (solid, liquid, gas), the element(s) to be detected and their concentration, the degree of heterogeneity of the samples, the purpose of the study, and the available instrumentation. In this report, only analytical techniques employing X-rays, both as primary

exciting radiation and emitted/scattered radiation, will be considered and discussed. The use of X-rays for the analysis of trace elements at low concentration has dramatically expanded the information available to scientists and stakeholders to determine the beneficial and detrimental fate and transport of trace elements in organisms and the environment.

X-rays are electromagnetic radiation with a wavelength between 10^{-11} and 10^{-8} m, corresponding to energies between 100 keV and 100 eV. Because of their short wavelength (comparable to the size of atoms) and high energy, they can penetrate tens to hundreds of micrometers into most materials and give rise to a number of physical phenomena that allow the determination of their chemical composition and structure.

For example, when X-rays impinge on a sample, elastic scattering in the form of single-crystal diffraction, powder diffraction, or coherent diffraction reveals atomic structure information and can be measured by X-ray-sensitive detectors. Inelastic scattering can be observed by either energy or wavelength dispersive detectors to determine the elemental composition and chemistry. X-ray absorption spectroscopy can be used to determine nearest-neighbour atoms structures and local chemistry. In addition, the penetrating power of X-rays allows for studies in three dimensions (3D) without physical sample sectioning or similar disruptive operations and is a key factor in several environmental studies [8].

Four main distinctive features characterize X-ray-based analytical methods: i) non- to minimally-destructive nature, ii) multi-elemental capability, iii) limited or no sample preparation requirement, and iv) spatially-resolved (in both two (2D) and three dimensions (3D)) analyses. These features allow X-ray based techniques to meet the complex needs of modern environmental scientists in studying trace elements in complex heterogeneous environmental media, under *in situ* conditions and at environmentally relevant concentrations [9, 10].

A number of X-ray based techniques are now available in many laboratories around the world, both as equipment built in-house and as commercial instruments. Limitations in sensitivity can be overcome in some cases by the use of high flux synchrotron sources. The continuous improvement of synchrotron light sources and X-ray beamlines has allowed for the investigation of extremely dilute elements in complex environmental samples around the world. Recently some of the most original environmental research studies have been significantly enhanced by incorporating synchrotron radiation-based X-ray technique(s) [11]. The high brightness of synchrotron sources may increase the risk of radiation damage occurring, especially in biological samples and organic compounds [12]. In addition, as demand for access to synchrotron techniques by environmental scientists continues to rise, it is becoming increasingly difficult to obtain beamtime at these facilities. Significant developments have been introduced in laboratory instruments which permit basic X-ray analyses on environmental samples.

Among their applications, X-ray techniques gave a remarkable contribution to the understanding of the biogeochemistry of nutrient and contaminant elements in environmental media, as well as their speciation and behaviour under different conditions and at multiple length scales. An important feature of X-ray methods is the possibility to integrate spectroscopic analyses at multiple length scales, from the millimetre to the submicron size, allowing the investigation of trace elements in highly heterogeneous environmental media where inorganic and organic compounds coexist with biota, water, and air, such as in soils and sediments [11, 13].

In recent years, third generation synchrotrons and X-ray free electron lasers capable of measuring femtosecond reactions have expanded our knowledge of fundamental chemical events, such as electron transfer, bond breaking/formation, and excited-state formations [14]. Understanding fundamental chemistry has real world consequences, for example, improving the manufacturing and efficiencies of materials (*e.g.* solar cells) affected by trace element impurities [15]. Synchrotron-based technologies are constantly being improved and will continue to elucidate the chemistry of life and environment.

In this report, following a brief description of the basic principles of the most common X-ray based techniques, a survey of both laboratory and synchrotron instruments will be presented, including their applications to different types of environmental matrices, such as air, water, soil, sediments, plants, living organisms, geological samples, and wastes. X-ray based imaging (2D and 3D) and microscopy techniques are also described and compared.

2 Basic principles

2.1 X-ray physics

The main analytical methods that make use of X-rays [16] discussed in this paper are X-ray fluorescence analysis (XRF), X-ray diffraction (XRD), and X-ray absorption spectroscopy (XAS). In addition, the use of X-ray computed microtomography (XCMT) for investigation of the 3D structure of materials is addressed.

XRF, XAS, and XCMT are based on the photo-electric effect, *i.e.* the absorption of an impinging X-ray photon by an atom, giving rise to the emission of a photo-electron that leaves an (inner) shell vacancy behind. Secondary processes that fill the vacancy are electronic transitions, some of which result in the emission of characteristic X-rays called fluorescence (depending on the core vacancy and Z of the element). This is illustrated in Fig. 1 as process B. In the primary energy (E_0) range from 10–100 keV, the photo-electric effect is the most important type of interaction between X-rays and matter. Figure 1 also depicts the alternative ways in which X-rays may interact with matter. Process A corresponds to the unhindered passage of the primary X-ray photon, *i.e.* transmission. Process C, called Rayleigh scattering, is the result of the coherent interaction of the totality of the electrons in the atom with the X-ray photon. It involves a change in direction of the original wave, while its energy/wavelength is conserved (elastic scattering). X-ray diffraction results from the interference of Rayleigh-scattered X-rays of periodically spaced atoms. In process D, called Compton scattering, a single (weakly bound) electron exchanges energy and momentum with the impinging photon, causing it to become ejected from the atom as a recoil electron. This process changes the direction and energy of the X-ray photon; its final energy (E_s) depends on the scattering angle θ.

The relative magnitude of processes B–D is expressed by their respective cross sections $\sigma_{\text{photo-el.}}$, σ_{Coherent}, and $\sigma_{\text{Incoherent}}$, the sum of which, multiplied by the ratio of the Avogadro constant ($N_A \approx 6.02252 \times 10^{23}\ \text{mol}^{-1}$) and the molar mass M of the material (in g/mol), is called the mass attenuation coefficient $\mu_m = (\sigma_{\text{photo-el.}} + \sigma_{\text{Coherent}} + \sigma_{\text{Incoherent}})\, N_A/M$, which is a quantity that depends on both the atomic number and the photon energy. The mass attenuation coefficient of a multi-element material is given by $\mu_m = \Sigma_i w_i \mu_{mi}$, where μ_{mi} is the mass attenuation coefficient of the i^{th} elemental constituent and w_i its mass fraction. The transmitted intensity I_t of a beam of monochromatic X-rays through a foil of a material of thickness d and density ρ is given by Beer's law:

$$I_t = I_0 \exp[-\mu_m(E_0)\rho d] \tag{1}$$

where I_0 is the original intensity of the beam with energy E_0. The product $\mu_m \cdot \rho$ is called the linear attenuation coefficient (μ).

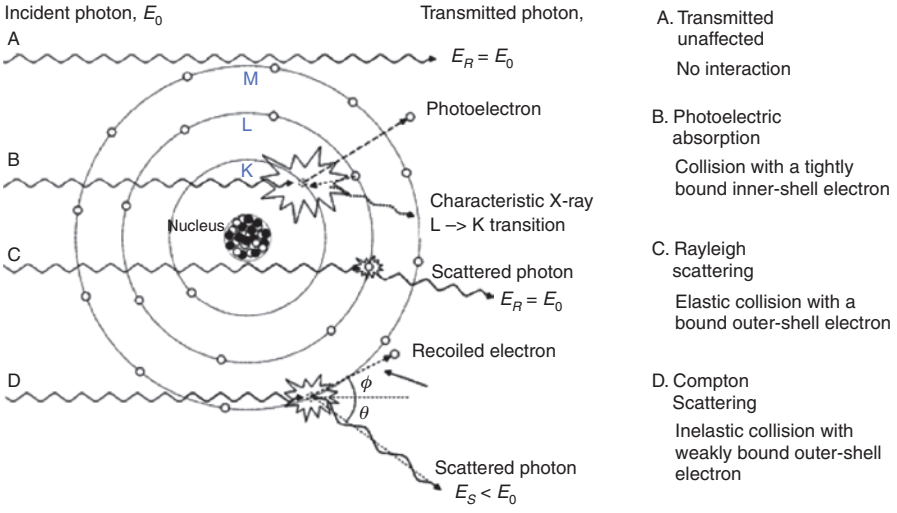

Fig. 1: Interaction processes of X-rays with matter.

2.2 X-ray fluorescence analysis and related methods

XRF analysis is a powerful analytical tool for the spectrochemical determination of many of the elements present in a sample [17]. The emission of element-specific characteristic radiation, X-ray fluorescence, is induced when photons of sufficiently high energy remove inner shell electrons from their atom by the photoelectric effect, creating electron vacancies in inner shells (K, L, M, …; see Fig. 2). The creation of a vacancy in a particular shell results in de-excitation within 100 fs *via* a cascade of electron transitions, correlated with the emission of secondary (X-ray) photons and secondary electrons. The emitted photons have a well-defined energy corresponding to the difference in energy between the atomic shells involved. Not all relaxation transitions of electrons from outer shells or subshells to the core vacancy are allowed, only those obeying the selection rules for electric dipole radiation. The family of characteristic X-rays, corresponding to the element's transitions, allows the identification of the element. Next to this radiative form of relaxation, a competing process involves the emission of secondary electrons. In this process, the core vacancy is filled by electrons from higher atomic shells, but instead of emitting secondary photons, the transition energy associated with this relaxing electron is imparted to another electron, which is then itself emitted. This emitted secondary electron is called an Auger electron. This process will not be discussed further here.

XRF analysis is achieved through the measurement of wavelength or energy and intensity of the characteristic photons emitted from a sample. This allows the identification of the elements present in the sample and the determination of their mass or concentration. All the information for the analysis is stored in the measured spectrum, which is a line spectrum with all characteristic lines superimposed above a certain fluctuating background (Fig. 3). Other interaction processes, mainly the elastic and inelastic scattering of the primary radiation on sample and substrate, contribute to the background.

Measurement of the spectrum of the emitted characteristic fluorescence radiation is performed using wavelength dispersive (WD) and energy dispersive (ED) spectrometers. In wavelength dispersive X-ray fluorescence analysis (WDXRF), an intensity spectrum of the characteristic lines *versus* the wavelength or diffraction angle (2θ degrees) is measured with a Bragg single crystal as the dispersion medium, while counting the photons with a detector, a Geiger-Müller, or a proportional or scintillation counter (Fig. 3a). In energy dispersive X-ray fluorescence analysis (EDXRF), a solid-state detector is used to count the photons, simultaneously

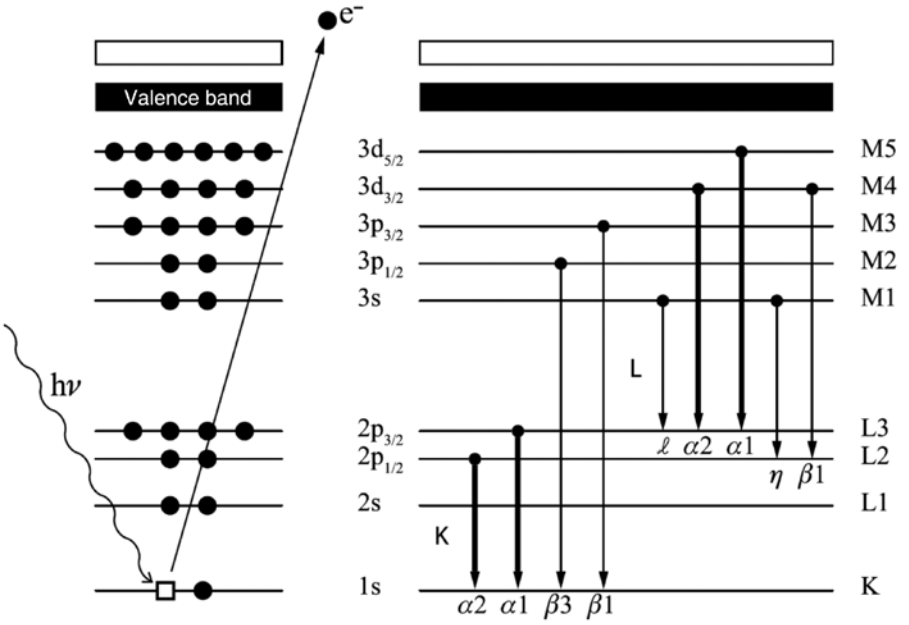

Fig. 2: Inner shell ionization and photo-electron emission (left panel) is quickly followed by one of several electronic transitions (right panel) that serve to fill up the vacant spot left by the photo-electron.

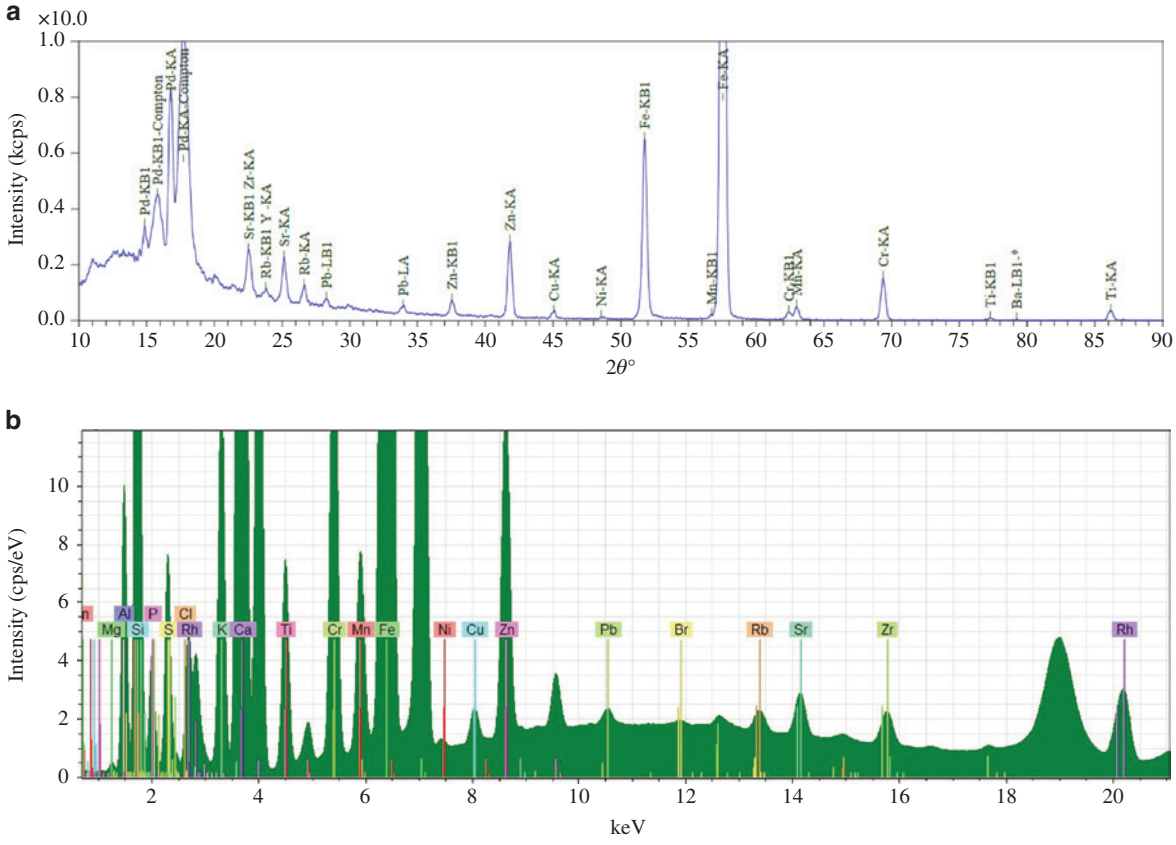

Fig. 3: (a) WDXRF spectrum of a metal-polluted soil. X-ray source anode: Pd. (b) EDXRF spectrum of the same polluted soil as in (a). X-ray source anode: Rh. Spectra collected at Micro X-ray Lab, University of Bari, Italy.

sorting them according to energy and storing the result in a multichannel memory. The result is a spectrum of measured intensity as a function of X-ray energy (Fig. 3b).

The range of detectable (naturally occurring) elements ranges from Be ($Z = 4$) to U ($Z = 92$). The concentrations that can be determined with standard spectrometers of a WD or ED type lie in a wide dynamic range: from parts per hundred down to μg g^{-1} [18]. In terms of mass, the nanogram quantification range is reached with spectrometers having the standard excitation geometry (90° angle between detector and incident photons). Using a special incident photon geometry impinging on the sample surface near the angle of total reflection—a method called total reflection XRF (TXRF)—sensitivity can be obtained to the femtogram (10^{-15} g) scale using synchrotron photon sources [19]. In general, TXRF may allow for the detection of concentrations below the μg g^{-1} level, which is usually the limit for XRF analyses [19].

2.3 Microscopic elemental analysis: μ-XRF, EPMA/SEM-EDX and μ-PIXE

When the creation of inner-shell vacancies is realized by means of electron or proton bombardment, then the corresponding analytical method is called Electron Probe Micro Analysis (EPMA), Scanning Electron Microscopy coupled to energy dispersive X-ray analysis (SEM-EDX) [20], or Proton Induced X-ray Emission (PIXE) [21]. Since these methods involve excitation using charged particle beams that are relatively easy to focus into a small spot, they have evolved naturally towards X-ray based microanalysis of materials. The microscopic equivalent of XRF, μ-XRF, has developed in only the last two decades, thanks to the increasing availability of highly brilliant X-ray sources and microfocussing X-ray optics. The evolution of more compact and larger area energy-dispersive X-ray detectors have benefitted (μ-)XRF, EPMA, and (μ-)PIXE.

When used in combination with X-ray tubes, μ-XRF allows absolute detection limits in the picogram range to be obtained for thin samples. In massive samples, relative limit of detection (LD) values around 10 μg g^{-1} have been reported. At synchrotron facilities, the capabilities of the μ-XRF method (both regarding spot sizes and detection limits) are significantly better: 10^{-15} to 10^{-18} g absolute detection limits are obtained with beams that are between 0.1 to 2 μm in diameter. Using monochromatic beams of polarized radiation leads to optimal peak-to-background ratios in the resulting EDXRF spectra, resulting in relative LD values in the (1-100) ng g^{-1} range for biological materials [22].

The application of μ-XRF to a great variety of problems and materials has been described, including geochemistry, engineering, biology, industrial, and environmental studies [23]. The fact that quantitative data on (trace) constituents can be obtained at the microscopic level without sample damage is especially of use in many different circumstances. At synchrotron sources, (μ-)XRF investigations of heterogeneous materials are also frequently combined with other methods, such as XAS and XRD, providing speciation information (*e.g.* element oxidation state and coordination, correlation with other elements and/or mineral phases) on major, minor, and/or trace constituents.

2.4 Quantitative aspects of X-ray analyses

Since the interaction of individual X-ray photons of a specific energy with individual atoms of specific atomic numbers can be very well-described theoretically, in principle any X-ray-based analytical method has the potential to be used for quantitative analysis [24].

Quantification approaches in X-ray analyses are either based on the use of extensive sets of calibration standards (that are similar to the materials to be investigated) and empirical calibration models, or they make use of theoretical models that describe the interaction between X-rays and matter. These theoretical models allow the use of a smaller number of calibration standards. Some approaches, called “standardless”, claim that quantitative analysis is possible without any calibration standard.

WD-XRF and ED-XRF are now very reliable analytical tools for the quantification of trace elements in environmental samples, especially when appropriate empirical calibrations are performed. Semiquantitative analyses based on fundamental parameters mathematical methods [25] or Monte Carlo simulations [26] are very useful when only few standards are available. Similar approaches can be applied also to PIXE [27] and electron-probe spectroscopies [28].

With X-ray microanalyses, which are normally employed to obtain information on the local elemental composition of inhomogeneous samples, additional problems must be taken into consideration, mainly (i) the heterogeneous nature of both the unknown materials and those used for calibration; and (ii) the fact that the primary beams penetrate relatively deeply below the surface of the samples, yielding a depth-averaged signal.

As a result, in many cases, quantitative results obtained with X-ray microanalyses are semi-quantitative in nature and are associated with relatively large errors. However, the uncertainty in quantitative results can be reduced via the development of (i) new irradiation/detection strategies and associated quantification strategies, (ii) new calibration standards, and (iii) specific solutions for particular applications. In the case of μ-XRF, the contribution of these developments towards more accurate quantitative determination has been extensively discussed by Janssens *et al.* [23].

2.5 X-ray absorption spectroscopy

XAS is a powerful technique that provides information regarding the chemistry of an element in basically any matrix, ranging from solid state, such as minerals, to soft matter, such as biological specimens, to solutions and amorphous states, such as glasses, and to gases. The energy position and the resonant and oscillatory pattern of an XAS spectrum provide information on the absorbing atom’s oxidation state and on its electronic structure and coordination or near-neighbour structure with an accuracy in interatomic distances

within 0.02 Å, coordination numbers within ~20 %, and neighbour atom type identification within $Z \pm 1$. The reader is referred to a very recent comprehensive publication on XAS and emission spectroscopies [29] and a review [30].

In an XAS experiment, changes in the linear absorption coefficient (μ) of an element in a sample is measured as a function of incident photon energy (see an example in Fig. 4). XAS requires a highly monochromatic (with $\Delta E/E \approx 10^{-4}$ to 10^{-5}), high flux X-ray beam. The photon intensity of the incoming beam is recorded before the sample (I_0) and the transmitted intensity after the sample (I_t) for different monochromatic photon energies; for a given sample length (d), the absorption coefficient is given by rearrangement of Beer's law (Eq. 1) given above ($\mu(E)d = \ln[I_0(E)/I_t(E)]$) (see note below).[1] Instead of registering the transmitted photon intensity, I_t, in what is referred to as standard transmission geometry, one can also measure the intensities of proportional secondary processes, such as fluorescence emission (indicated in Fig. 4a) or the emission of secondary electrons, using appropriate detectors. In these cases, the absorption, $\mu(E)d$, is proportional to the ratio of emission to incident photon intensity. In a XAS spectrum, a significant change above the background in μ, referred to as its absorption edge, is observed at the absorbing element core state threshold or ionization energy, E_t. This represents the amount of energy needed to remove an inner shell electron through the photoelectric effect. The value of E_t is specific to that element and associated electron transition, which renders the XAS technique element specific. In a manner similar to XRF, these edges are referred to according to the principal quantum number of the electron being excited, *i.e.* K, L, M, *etc.* absorption edges.

As is evident in Fig. 4b, above the Cu K absorption edge is the oscillatory structure of μ. These oscillations result from the scattering of the excited photoelectron on surrounding atoms. Based on the scattering processes responsible for this structure, the photon energy range in an X-ray absorption spectrum is generally divided into two regions: the X-ray absorption near edge structure (XANES), at lower energies, and the extended X-ray absorption fine structure (EXAFS), at higher energies. The XANES region often exhibits resonant features associated with photoelectron transitions to unoccupied bound states near the absorption edge, in what is called the pre-edge region.

In the EXAFS region, the wave function of the excited photoelectron in the core region is modulated by interference of the outgoing wave with one that has been backscattered on surrounding neighbouring atoms. In this sense, the EXAFS oscillatory pattern is quite literally an interferogram of the atomic arrangement surrounding the absorbing atoms. It therefore contains metrical parameters characterizing this arrangement, including the number and type of neighbouring atoms and their distance to the absorbing atom. Constructive interference between outgoing and backscattered waves leads to maxima in the EXAFS, while destructive interference leads to minima. One might intuitively predict that the distance between the absorbing atom and its backscattering neighbours (R) and the kinetic energy (or wavelength) of the photoelectron (see note below)[2] are determinant in the periodicity of the interference and this is indeed the case. The EXAFS can be described as a dampened harmonic oscillator using the following equation

$$\chi(k) = \frac{S_0^2}{k}(-1^{\ell})\sum_j N_j \left| f_j(k,\pi) \right| \frac{e^{-2R_j/\lambda(k)}}{R_j^2} e^{-2k^2\sigma_j^2} \sin\{2kR_j + \Phi(k, R_j)\} \quad (2)$$

where N is the coordination number, $f(k)$ the backscattering amplitude function for the neighbouring atom type, $\Phi(k,R)$ the total phase shift of the photoelectron as it transverses the atomic potentials of the absorbing and backscattering atoms, S_0^2 the amplitude reduction factor accounting for multi-electron shake-up and shake-off effects, ℓ the angular momentum quantum number, σ^2 the mean square average displacement from the average bond length, and $\lambda(k)$ the mean free path length of the photoelectron. The sum in Eq. 2 is over each coordination shell j up to the n^{th} coordination shell, typically up to distances of 5 Å. Equation 2 has

1 Note: Although one could theoretically use the measured absorption and a calibrant to determine elemental concentration in the sample, as a general rule the height of the absorption edge in the course of data analysis is normalized to unity, so that one can easily compare spectra of different samples.

2 Note: The photoelectron kinetic energy is the difference between the incident photon energy and E_t.

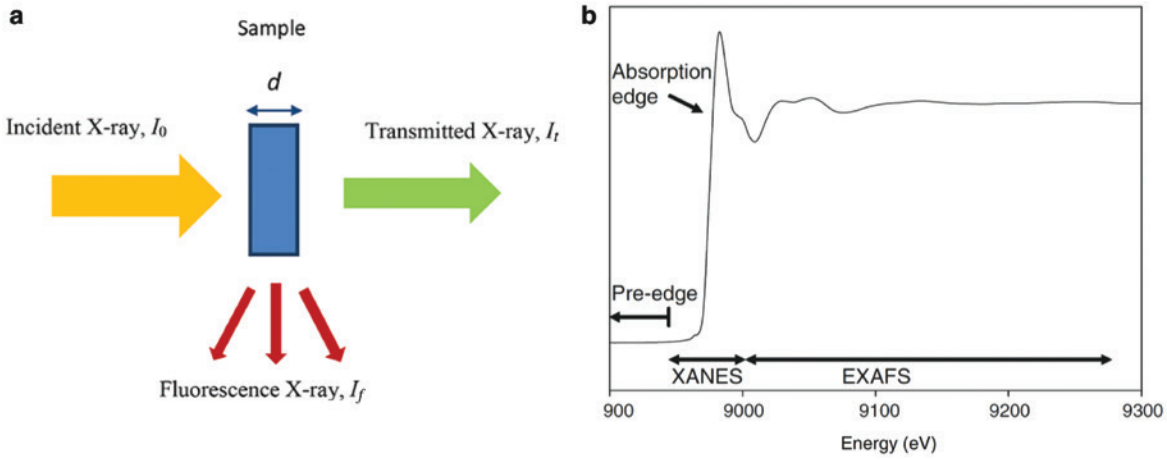

Fig. 4: (a) Experimental arrangement for X-ray absorption spectroscopy (b) Cu K XAS spectrum of malachite [$CuCO_3.Cu(OH)_2$] showing the region of the spectrum pertinent to XANES and EXAFS.

essentially two terms, a phase term $\sin(2kR + \Phi(k,R))$ and a remaining amplitude term. The functions $f(k)$ and $\Phi(k,R)$ are unknown, are dependent on backscattering atom type, and must be either extracted empirically using EXAFS data from model compounds of known structure or theoretically calculated. That $\Phi(k,R)$ and $f(k)$ are dependent on the backscatter type allows for the identification of elements comprising a coordination shell, providing the types of atoms differ sufficiently in Z; neighbouring atoms (Z, $Z+1$) have similar functions and cannot be differentiated. Note that Eq. 2 assumes that the photoelectron can be approximated by a plane wave and that the sample has a minimum of disorder (Gaussian pair distribution). EXAFS data are analysed (following the conversion of photon energy to photoelectron wave vector (k), background removal, and normalization) by fitting experimental data with Eq. 2 using iterative least square fit techniques. The parameters obtained describe the coordination structure of the absorbing atom.

The pre-edge and XANES regions extend to energies around 50 to 100 eV above E_t. As E_t is situated in the XANES region, the energy position of XANES resonant features at the absorption edge give insight into the average valence state of the absorbing atom type in a sample. As in the EXAFS regime, the changes observed in μ within the XANES region above E_t also result from the scattering of the photoelectron on neighbouring atoms; however, at low energies $\lambda(k)$ is large and the photoelectron is not only backscattered but scattered in all directions numerous times. This multiple scattering (MS) character of XANES renders it sensitive to the coordination geometry of the absorbing atom. However, this MS character makes a theoretical treatise more complicated; as a result there is no simple XANES equation. Typically, two strategies are used to interpret XANES spectra: 1) "Fingerprinting", or the comparison of XANES features in spectra of unknowns with that of known compounds; 2) the calculation of theoretical XANES under a variation of specified parameters, *e.g.* sample orientation or atomic cluster size, to explain observed trends in experimental data.

As an illustrative example, Fig. 5 shows the technetium K XANES for technetium dispersed in cement following the addition of reductants compared to the fingerprints for technetium(VII) and technetium(IV) compounds. The pre-edge associated with the technetium(VII) spectrum (shown highlighted) and the shift in edge energy are used to monitor reduction. Theoretically, calculated spectra (and other fingerprinting studies) have shown this pre-peak to be indicative of photoelectron transitions to empty frontier orbitals for d-metals with tetrahedral coordination. The technetium originally in the cement samples was tetraoxidotechnetate(VII), having technetium(VII) coordinated to four oxygen atoms in tetrahedral symmetry. The technetium K XANES spectrum for Cement 1 with no added reductant is therefore similar to the technetium(VII) reference compound, showing a strong pre-edge resonant feature. Cement 3, with added Na_2S as reductant, no longer exhibits a pre-peak and has an edge energy position comparable to the spectrum for the technetium(IV) reference, allowing the interpretation that complete reduction of technetium(VII) to technetium(IV) occurred in this sample. The XANES for Cement 3 also exhibits weaker MS structures at the

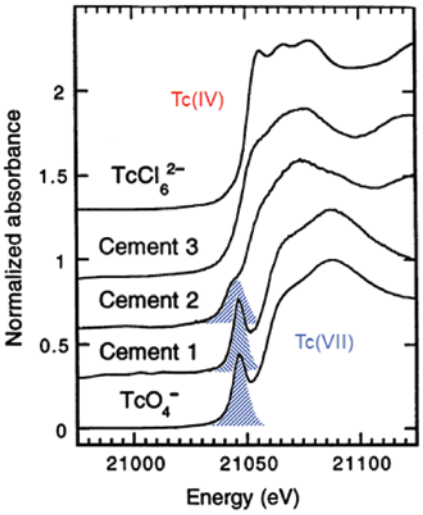

Fig. 5: Technetium K XANES measured for cement samples containing tetraoxidotechnetate(VII) without additives (Cement 1), added blast-furnace slag for partial reduction (Cement 2) and added Na_2S for complete reduction (Cement 3), compared to known reference compounds containing technetium(IV) (top) and technetium(VII) (bottom).

maximum absorption compared to that for the technetium(IV) reference, indicating that the technetium(IV) in the cement sample is less ordered structurally. A pre-edge peak in the XANES of Cement 2, containing added blast-furnace slag as reductant, remains, but its intensity is diminished. The technetium K edge is also shifted to lower energy. Both these observations indicate only partial reduction of technetium(VII) to technetium(IV) in Cement 2.

2.6 X-ray diffraction

Crystalline materials contain 3D arrays of regularly spaced atoms. X-rays are waves of electromagnetic radiation with wavelengths in the atomic size range: 10^{-10} m = 1 Å. When the X-ray waves impinge on an atom, via elastic or Rayleigh scattering, the cloud of electrons around each atom can scatter these incoming waves, giving rise to secondary spherical waves emanating from each scattering electron. A regular array of scatterers produces a regular array of spherical waves. These waves will cancel each other out in most directions through destructive interference; however, in a few specific directions that depend on the orientation of the scattering crystal's principal axes and the spacing between the crystal's atomic planes, constructive interference will take place. All (series of parallel) atomic planes in the crystal can be thought of as collections of scatterers constructively contributing to a diffracted beam that is formed in a direction as if reflected by that (series of) plane(s) (see Fig. 6a). Bragg reflection takes place only for those angles fulfilling Bragg's law:

$$n\lambda = 2d \cdot \sin\theta \tag{3}$$

where d is the spacing between diffracting planes, n is an integer representing the diffraction order, and λ is the X-ray wavelength. Here θ corresponds to the angle that the incident beam makes with the crystal plane(s). The total scattering angle is 2θ. In cases where a single crystal is examined, this directional specificity gives rise to diffraction spots on an X-ray sensitive image detector or plate (Fig. 6b). X-rays are very suitable for producing diffraction patterns because their wavelength λ is typically of the same order of magnitude (1 to 100 Å) as the interplanar spacing in the crystal. In polycrystalline material circular Debye-Scherrer patterns are recorded instead of patterns of isolated spots. From the positions/diameters of these patterns, information on the atomic positions within the unit cell of the single crystal and on the different distances between the diffraction planes can be obtained [31].

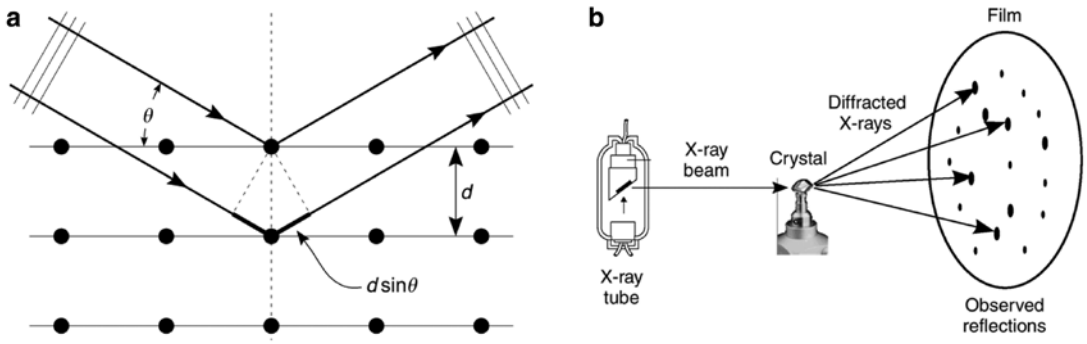

Fig. 6: (a) Bragg reflection by a set of parallel planes with interplanar distance *d*. (b) Experimental setup for X-ray diffraction, showing pattern of single crystal reflection.

2.7 X-ray Micro Tomography

Starting with the discovery of X-rays, the penetrative character of X-rays has been exploited to produce shadow images of heterogeneous objects, including human body parts. A non-destructive inspection that is optimized to the absorption contrast in a single transmission projection image in order to distinguish the inner structure of irradiated objects is called X-ray radiography. Its 3D equivalent, X-ray tomography, makes use of an extended series of projection images recorded under many different angles between the object and the primary beam. The object rotates around an axis perpendicular to that of the source-detector while a (large) series of shadow images are recorded by means of a suitable X-ray sensitive camera (Fig. 7). Mathematical reconstruction then allows for the creation of a virtual, 3D rendition of the object's shape and (inner) density variations, and to visualize its inner parts without physically sectioning or otherwise destroying it. This can be done both at the macroscopic (decimeter to meter) level, *e.g.* in medical computed tomography, as well as at the microscopic level.

Several manufacturers offer table-top X-ray computed microtomography (XCMT) instruments with an effective spatial resolution typically situated in the 0.1 to 10 micrometre range. This type of instrumentation usually makes use of cone-beams to illuminate the material under study. At synchrotron facilities, on the other hand, quasi-parallel beams are usually employed. In addition to making use of absorption contrast, where a transmission detector records the amount of radiation that is absorbed inside the irradiated object, phase contrast can also be exploited [32]. This utilizes enhanced edge-contrast caused by interference between the original X-ray beam and its refracted equivalent. In slightly absorbing materials, this significantly improves the clarity with which the interfaces between various material phases may be visualized. XCMT has been successfully applied in many fields, such as engineering, chemistry, soil science, and biology.

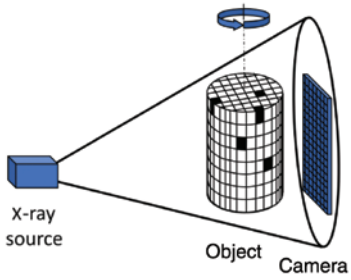

Fig. 7: Principle of cone-beam X-ray tomography.

2.8 X-ray sources, optics and detectors

Today, X-rays can be produced in a variety of manners suited for the generation of X-ray beams and microbeams, either using laboratory X-ray sources or at synchrotron radiation facilities. At synchrotrons, the dimensions of the primary beams used in hard X-ray microprobes are constantly shrinking. Currently (in 2018), beams of sufficient intensity with *ca*. 30 nm diameter can be produced using various optical technologies, while the smallest X-ray beams are on the order of 5 nm [33].

2.8.1 Laboratory sources

In the laboratory, three different types of X-ray sources can be employed: (a) sealed X-ray tubes and (b) rotating anode tubes are the most commonly employed, while (c) primary X-rays produced in radioactive sources are also still utilized to a lesser extent. In most X-ray tubes, X-ray generation is realized by accelerating electrons to tens of kV and forcing them to decelerate rapidly when they impinge on a solid block of metal. Sealed X-ray tubes exist today in a variety of shapes and power-settings, ranging from very compact sources, *e.g.* those that can be integrated into portable equipment, to heavy duty, high voltage varieties suitable for the generation of X-rays up to 600 keV. Commonly employed anode materials are Cu, Mo, and W, but other high melting materials such as Cr, Rh, Pd and Ag are also popular. Some manufacturers also offer X-ray tubes with Co and Fe anodes. The power of fixed anode X-ray tubes can go up to 2 kW, while that of micro-focus sources is typically on the order of 30 to 50 W. In the latter type, the electron beam is fixed onto a small spot (typically 30-50 μm in diameter) on the anode block. The smaller the focal spot, the lower the maximum power at which the tube can be used without inflicting burn-in damage to the anode surface. In rotating anode X-ray tubes, a higher power density can be achieved by employing a rotating metal cylinder instead of the stationary anode. During each revolution, only a small part of the anode is in the electron beam, producing X-rays, while the rest can cool down [34]. An interesting new development is liquid metal jet sources, where a ribbon of molten metal (*e.g.* Ga, Sn) rather than a rotating cylinder of solid metal serves as anode. The liquid state of the anode allows for more efficient heat dissipation and, in combination with optimized electron optics in the X-ray tube, results in a more brilliant X-ray source [35]. Inverse Compton sources constitute another type of X-ray source situated halfway between conventional X-ray tube sources and synchrotron facilities. In these sources, X-ray generation is realized through the interaction between laser light and a highly energetic electron beam. Electron beams can be formed by impinging a high-power laser onto a pulsed gas jet and accelerating the generated plasma electrons in the laser wakefield having a high field gradient. If the accelerated electrons overlap spatially and temporally with ultrafast laser pulses in the visible range, the electrons scatter in a manner similar to an undulator insertion device at a synchrotron, but with a higher frequency (that of optical light, as opposed to undulator magnet spacing), allowing for a compact source and the possibility of tabletop spectrometers [36].

2.8.2 Synchrotron X-ray sources

In a number of specialized cases, X-ray analytical methods also make use of synchrotron sources. Synchrotron radiation (SR) is produced by high-energy (GeV) relativistic electrons circulating in a storage ring. This is a very large, quasi-circular vacuum chamber where strong magnets force the particles on closed trajectories. X-radiation is produced during the continuous acceleration of the particles. SR-sources are several (6 to 12) orders of magnitude brighter than X-ray tubes, have a natural collimation in the vertical plane, and are linearly polarized in the plane of the orbit. The spectral distribution is continuous. Since the SR originates from a source point of small dimensions and is released in a very narrow angular range, it is easily focusable into micro- and/or nanobeams. An additional advantage is the high degree of polarization of SR, causing spectral backgrounds due to scatter to be greatly reduced when the XRF detector is placed at 90° to the primary beam

and in the storage ring plane (standard geometry). The combination of a high primary beam intensity and low spectral background reduces LD values of SRXRF to the ppb level. More details about synchrotron X-ray sources and applications are reported in Section 3.

2.8.3 X-ray microfocussing optics

The introduction and maturation of different types of (compact) X-ray optics has made the development of laboratory- and synchrotron-based hard X-ray micro and nanoprobes possible. Most, if not all, synchrotron facilities worldwide now are equipped with at least of one hard X-ray microprobe beamline, where a combination of μ-XRF, μ-XAS and/or μ-XRD measurements can usually be performed simultaneously on the same material. In addition, in some cases, a combination with other methods, such as small angle X-ray scattering (SAXS) or various forms of X-ray micro/nanotomography, have been realized.

Four major types of X-ray focusing optics (Fig. 8) based on reflective or refractive focusing are currently being employed, mostly at synchrotron sources: (a) one dimensionally-curved mirrors based on total reflection of the X-rays, usually in a Kirk-Patrick Baez geometry (KB optics) [37]; (b) compound refractive lenses (CRL) [38]; (c) (poly)capillary (PC) optics (also based on total external reflection) [39]; and (d) Fresnel-Zone plates (FZP), based on interference phenomena of refracted X-ray wave fronts transmitted by a patterned mask [40]. A more recent type of X-ray optics suitable for synchrotron sources are multilayer Laue lenses (MLL) [41]. Of the above-mentioned microfocussing technologies, only (poly)capillary X-ray lenses are frequently used in combination with laboratory X-ray instrumentation.

In recent years, the technique of confocal μ-XRF has been developed, where a secondary optic placed between the sample and detector prevents all XRF radiation, except that originating from a specific depth below the surface of the sample, from reaching the detector. This allows for an analysis of heterogeneous samples in three dimensions, with a resolution of *ca*. 10 to 50 μm [42–44].

2.8.4 X-ray detectors and cameras

With respect to the devices for energy-dispersive detection of X-rays, two important evolutions are worth mentioning. The first is a general move from traditional solid state (Si(Li), Ge(Li), *etc*.) detectors requiring permanent maintenance at liquid nitrogen temperatures towards more compact Si-PIN diodes and Silicon drift diodes (SDD) that are thermo-electrically cooled [45]. The second is the recent development of few- to multi-crystal detector arrays (*e.g.* Maia detector) [46] and energy-dispersive X-ray cameras [47, 48], allowing the detection of fluorescence radiation in a much larger solid angle than previously possible. The Maia detector, which consists of an array of 384 photodiode detectors and associated signal processing, is closely

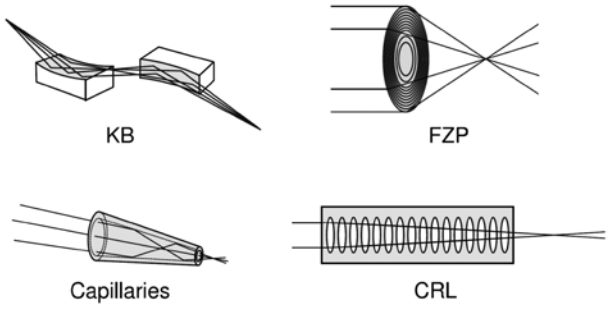

Fig. 8: Four types of commonly employed X-ray optics: (clock wise from upper left): curved mirrors in KB geometry, Fresnel zone plate lenses, compound refractive lenses, and capillary optics.

coupled to a field-programmable gate array (FPGA)-based control and analysis system [46]. These developments open up new methodological possibilities, *e.g.* for large area element-specific mapping, either *via* fast sample scanning or by making use of full-field detection schemes [49].

3 Synchrotron techniques and instrumentation

Synchrotron radiation is ideally suited to trace element analysis in environmental samples for several reasons, including high sensitivity and low background due to the linear polarisation. The high brilliance of synchrotron radiation enables both focussing to small beams for high spatial resolution and extremely fast acquisition rates. Hard X-ray microprobes use the deep penetration of X-rays through matter to probe and search large volumes with spatial resolution efficiently and to enable tomography. X-ray fluorescence tomography is an important method for trace element analysis in biological tissues, particularly in combination with frozen hydrated samples.

X-ray Absorption Spectroscopy (XAS), when recorded using X-ray fluorescence signal, allows for chemical speciation of dilute systems in a dense sample matrix. XAS is routinely performed on bulk samples; however, with the advent of faster scanning and acquisition schemes, XAS can also be spatially resolved. Chemical speciation of trace elements by means of XAS is a uniquely synchrotron-based technique, as it requires incident X-ray energies or wavelengths that can be tuned. This is only possible for the characterisation of trace elements using monochromatic wavelengths selected from intense broad band synchrotron radiation to the required X-ray energies, which straddle the absorption edge of the element of interest. The ability to select incident excitation energy also allows unique flexibility within X-ray fluorescence microscopy. For example, it is possible to avoid signal from high concentration elements in a matrix by tuning the incident radiation below the relevant absorption edge of the high concentration element.

Ultimately, the brightness and tunability of synchrotron radiation offers versatility and fast acquisition, enabling either high sensitivity or high throughput. Sensitivity can be exceptionally high, especially for the first row transition metals. To give one example, the LD for zinc at leading edge facilities (*e.g.* ESRF ID16A) is $1.1 \cdot 10^{-18}$ g (see note below).[3]

3.1 Relevant synchrotron-based imaging techniques

In this section, discussion is limited to those techniques capable of trace element sensitivity, with particular attention paid to those that use X-ray fluorescence contrast. Other techniques that use absorption, diffraction, or scattering contrast are not always suitable for analysing trace element content, or they may have poor contrast. However, these techniques, such as X-ray absorption or phase contrast tomography, are often extremely useful for correlated studies, for example to understand the fine structural properties of a sample in which trace elements of interest occur.

Ptychography, a scanning coherent diffraction technique, is an emerging technique that can be used in parallel with scanning X-ray fluorescence microscopy and so is an ideal correlation technique. Ptychography can provide additional information about the structural environment of the trace metal(s) enriched structures.

The following synchrotron techniques will be briefly described in this section: scanning X-ray Fluorescence Microscopy (XFM) and related higher dimensional techniques, *e.g.* X-ray fluorescence tomography; XAS in fluorescence mode with spatial resolution, also as a scanning technique, alternatively described as

3 Note: In a thin carbon sample 5 μm thick, 10^4 zinc atoms can be detected with a 50 nm nanoprobe beam (incident flux of 10^9 photons per second at 10 keV, per-pixel time of 100 ms, detector solid angle of 0.2 sr), which gives 58 zinc fluorescence photons detected per 100 msec, representing 7.1 parts per million, and a mass of $1.1 \cdot 10^{-18}$ g (Jacobsen 2018, personal communication).

microspectroscopy, spectromicroscopy, or XANES imaging; as well as confocal X-ray fluorescence microscopy and related in-situ techniques that can provide a depth resolved or 3D characterisation of samples.

3.1.1 X-ray Fluorescence Microscopy

X-ray Fluorescence Microscopy (XFM) is a powerful technique to quantitatively determine and map element concentrations in a wide range of sample types. Specialised microprobes at synchrotron facilities can attain spatial resolution in the tens of nm, but more typically operate within the range from 200 nm to 10 μm [50]. The extended depth of focus of X-ray probes – ranging from several hundreds of μm to mm-scale – makes these probes ideal for addressing environmental science. Analysis depth is often determined by the penetration of the outgoing fluorescence X-rays, and therefore depends on the X-ray energy of the interrogated element and the overall specimen matrix composition.

X-ray beam energies (*e.g.* 5 to 25 keV) are employed to excite core level vacancies and promote hard X-ray emission, for which the fluorescence yield is high. The beam energy can be chosen to excite the suite of elements of interest, providing broad element coverage (typically from P to U), and is advantageous for detecting trace metals at sample depths beyond the reach of soft X-rays (below 3 keV). XFM typically uses an energy dispersive detector (*e.g.* SDD) at an angle of 90° to the incident beam to minimise scattered background. Increasing the detector solid-angle to maximize signal for a given dose increases the angular distribution of fluorescence X-rays [51], and so larger detectors have employed an annular geometry around the incoming beam (*e.g.* Maia detector), enabling the collection of fluorescence emission from a large solid-angle to be achieved, as well as freeing up the sample plane for both studies of large specimens and increased ranges of sample stage motion [52].

For example, XFM is capable of simultaneously mapping micronutrient elements (such as Ca, K, S), hyperaccumulated elements (such as Cd, Co, Ni, As, Se, Zn), and trace elements that are typically present in plants at far lower concentrations (such as Cu, Cr, Br) [52]. However, sensitivity is, among other things, dependent on the technical capabilities of detection systems. XFM beamlines commonly use single (or multi-element) germanium detectors (HPGe) and single (or multi-element) silicon drift detectors (SDD). SDDs can handle high count rates and have excellent energy resolution (*e.g.* 125 eV for manganese Kα), which can be advantageous for resolving line overlaps, whereas germanium detectors are primarily used for high-energy X-rays. However, these approaches tend to be limited in their minimum time per pixel, collection solid-angle, and count-rate capacity. The Maia detector uses a large detector array to maximize the detected signal and count rates for efficient imaging. Maia enables count rates up to about 10 megacounts s^{-1} and uses an annular detector geometry [53, 54]. This geometry enables a large solid-angle (1.2 steradian), while event mode data acquisition essentially eliminates readout delays. Together, these enable arbitrarily short pixel dwells (reaching below 100 μs). Sub-millisecond dwell times enable routine high definition imaging (10–100 megapixels) within a single shift of experimental access [55].

3.1.2 Spatially resolved X-ray Absorption Spectroscopy

While elemental co-localization and element associations provide useful information, XAS can illuminate the element-specific molecular-scale chemical information *in situ* within physically intact samples of any phase [56–58]. As described in Section 2.5, XAS measures the absorption of X-rays by a sample as a function of energy across the absorption "edge" of the element of interest.

Bulk XAS has been successfully applied to reveal the overall chemical speciation of Ni and other elements in plants [59–62], but local variations in speciation are difficult to detect, especially for species contributing to 5 to 10 % of the overall spectra. For example, Montargès-Pelletier *et al.* [61], found that citrate and malate were the main ligands responsible of Ni transfer within some hyperaccumulator plants by analysing different plant parts (leaves, stems and roots) *via* XAS. Spatially-resolved XAS approaches can determine the

variation in speciation that may occur over microns within tissues and at complex environmental interfaces, such as in the rhizosphere [63] and in oxidized pisolitic regolith [64].

XAS and XFM can be combined at suitable synchrotron facilities to provide information regarding the spatial distribution of different chemical forms of an element of interest. This is worthwhile when there is a mixture of chemical species within the sample with distinct localisations or contrasting spatial distribution, or where the size of the features of interest are comparable to the beam size [65]. In particular, XANES imaging can be employed to study samples with heterogeneous elemental concentrations and unknown chemical speciation variability. For example, Wang *et al.* [66] determined Se speciation in fresh roots and leaves of wheat (*Triticum aestivum* L.) and rice (*Oryza sativa* L.), showing that for plant roots exposed to selenium(VI) or selenium(IV), the majority of the Se was efficiently converted to C-Se-C compounds (*i.e.* methylselenocysteine or selenomethionine) and sequestered within the roots.

XANES maps are usually built up by "stacking" a series of XFM images, each collected with different incident X-ray energies, spanning the absorption edge of the element of interest. This is equivalent to the technique used in scanning transmission X-ray microscopy (STXM [67]). To be practical, 2D XANES mapping is contingent on the availability of extremely fast and efficient X-ray detection; otherwise, it is limited to situations where there are large spectral shifts in the XANES of species being investigated (*e.g.* where different oxidation states of As are present). For example, localising the different oxidation states of As in *Pteris vittata* [59] and of Se in *Astragalus bisulcatus* [68] has been successfully demonstrated with a limited number of energy-steps required due to the dramatic differences in energies of the different As/Se oxidation states. Recently, with ultra-fast detectors, full As K XANES spectra have been captured by registering stacks of μ-XRF maps collected at 81 energies spanning the 11.802 to 12.017 keV range in non-hyperaccumulator plants [69]. In a similar fashion, statistical analysis using principal component analysis and cluster analysis of image stacks collected *in vivo* across the iron K-edge allowed imaging of metal distributions and quantification of iron(II) and iron(III) content of nematodes [70]. XANES mapping also overcomes spatial drift problems that can arise when measuring XANES at a single point [65].

3.1.3 X-ray fluorescence tomography and confocal detection

The long penetration range of the characteristic X-ray fluorescence enables the acquisition of maps of the projected elemental content of thick samples. The absorption length of K-line X-ray fluorescence of light transition metals is several hundred micrometers in a hydrated matrix. In order to transfer the lateral size of the X-ray probe into lateral resolution of the scanned image, appropriate depth resolution is required. A common approach is to physically section the samples. However, this procedure can be challenging and prone to artefacts. The deep penetration length of X-rays can be utilized to probe the interior of objects selectively by 'virtual sectioning', namely by the use of computed tomographic reconstruction methods or confocal imaging. Virtual sectioning, in combination with cryo-fixation (for biological samples) of (small) samples, can be considered minimally invasive and allows the analysis of samples with sub-micron resolution close to their native state. X-ray Fluorescence Micro-Computed Tomography (XFM-CT) enables the reconstruction of 2D or 3D elemental data from a rotation series of projection images [71, 72]. The diameter of the sample for X-ray fluorescence tomography is limited to the penetration depth of the X-ray fluorescence of the element of interest. An advantage of tomography is that the image resolution of the virtual section after tomographic reconstruction can approach the size of the probing beam.

Confocal XFM, on the other hand, allows the measurement of specific sub-volumes within a specimen. Confocal XFM does not require a rotation of the sample, but instead employs a confocal optic to confine the field of view of the energy-dispersive detector so that the signal derives from only a small portion of the illuminated column [73] (*cf.* Section 2.8.3). A severe limitation of confocal XFM is that the depth resolution is limited by the confocal optic to, at best, several micrometers, making 3D imaging with confocal optics less attractive at synchrotrons, where sub-micron resolution is often required. However, confocal optics of high efficiency (polycapillary optics) have been used successfully for the collection of XANES spectra from

defined confocal volumes in a specimen [74]. For example, As speciation was measured for specific tissue structures separately within a complete leaf in the frozen hydrated state. With this approach, arsenate, arsenite, As-glutathione and As-phytochelatine complexes were identified, with varying ratios, within the leaf of the aquatic plant *Ceratophyllum demersum* [75]. Single voxel confocal XANES measurements are considered the most efficient way to obtain chemical speciation data at the tissue level from inside the sample without sectioning the sample or using complex extraction procedures.

3.2 Types of samples that can be analysed

X-ray techniques are extremely versatile and are uniquely placed to perform *in situ* studies. The basic types of samples that can be analysed range from rock to soils to biological tissues (plants and animals) and cells. Although not usually considered in the environmental science regime, metals, alloys, catalysts, and other hard materials can also be usefully studied. Hard X-rays enable measurements to be made in air, a helium atmosphere, or under a cryo-stream to maintain frozen specimens (see Fig. 9).

This enables, for example, measurements on small, or portions of large, live specimens. A specimen can be frozen *in situ* using a cryo-stream for samples up to about 3×3 mm in size.

Sample size limitations depend upon the detector geometry employed, the instrumental technique, and the sample matrix. For tomography, there is a limitation on the maximum sample diameter to ensure full penetration of the probe beam and adequate "escape" of the X-ray fluorescence, which becomes more critical for lighter elements, such as P and S. Typically, 100 μm is the maximum diameter if light elements are of interest. Additional efforts are needed to solve the self-absorption corrections required to accurately map lighter elements and correctly quantify their concentrations. For heavier elements this is less of an issue. For example, single slice tomography has been performed on a sample with diameter 1.0 mm [72] for As detection. Samples that naturally have a cylindrical shape, *e.g.* plant roots and stems, are ideal for tomography analyses. However, most of the samples can often be cut to the required shape and size, taking care that the

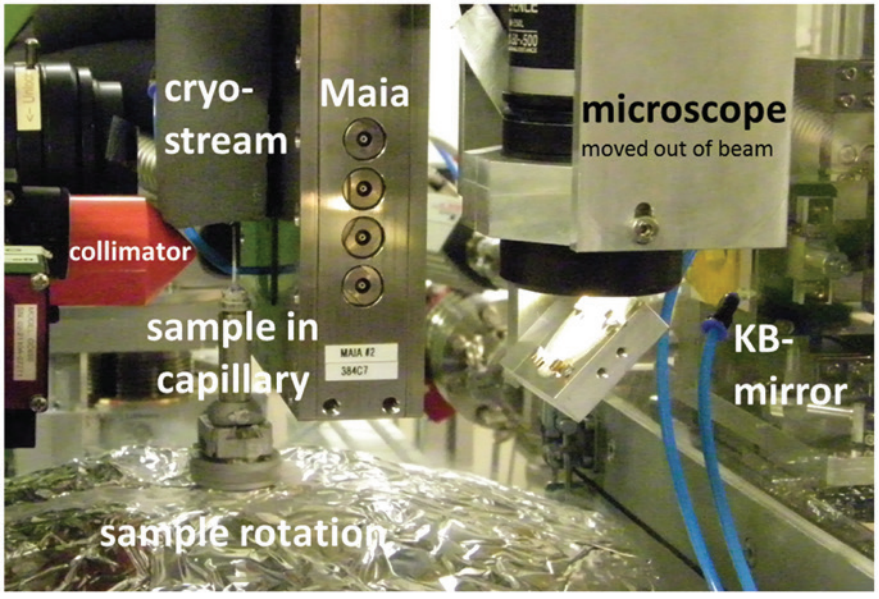

Fig. 9: Cryogenic X-ray fluorescence tomography set-up with Maia detector at the P06 Microprobe experiment (DESY, Hamburg, Germany). A plant tissue sample inside a capton capillary mounted on a magnetic sample holder was plunge-frozen and placed on the goniometer head under an FMB Oxford cryo-stream with custom-made nozzle extension. Piezo stages for centering the capillary, the air-bearing rotation and translation stages are covered with an Al foil for protection. Courtesy P06 Falkenberg/Küpper [72].

cut surfaces are omitted from the final analysis due to potential damage or trace element relocation and/or contamination.

X-ray analysis can be performed on exceedingly small sample volumes. For example, a 1 μm^2 incident beam illuminating a 20 to 40 μm plant sample thickness detects femtograms of the element of interest in absolute terms, which translates to 10 to 100 $\mu g\ g^{-1}$ local concentration in the plant tissue [65].

Fast, efficient, on-the-fly raster scanning can avoid prolonged X-ray exposure at each position on the sample and reduce the potential for radiation damage. Nonetheless, radiation damage is still the key limitation of the technique, given the requirement to repeatedly scan the sample at a number of incident energies, especially for XANES images, which can take many times longer to collect than standard XFM elemental distribution maps. Radiation damage can be mitigated by analysing dehydrated samples, as water mediates the redox processes involved, or by maintaining a frozen hydrated sample at cryogenic temperatures using a variety of approaches, such as nitrogen cold streams.

3.3 General overview of instruments and facilities

For more than 30 years, X-ray beamlines have been operated at almost every synchrotron. Initial experimental stations for scanning X-ray fluorescence imaging were supplemented by micro-XANES spectroscopies and micro-X-ray diffraction; different optics were used to focus into the micrometre range and below. Prominent pioneer beamlines were ESRF ID22 and NSLS X26A (KB optics), APS 2-ID-E and ESRF ID21 (FZP), and DESY beamline L (PC lenses). Over the years, advancements in synchrotron emittance and X-ray optics enhanced focussing capabilities drastically, by up to three orders of magnitude in resolution. The perfection of KB mirrors has been revolutionised by the invention of a new polishing technique (DESY P06 microprobe, P10 GINIX, ESRF ID21 ID16, MAXIV nanoMAX). Coating with Multilayers allows white beam operation and focussing into the 50 nm range and below with high flux (ESRF ID16). Zone plates have improved in structure, size, and especially in thickness for hard X-ray application (APS 2-ID-E, APS Bionanoprobe) [76]. MLL have matured as the instrumentation for focussing below 20 nm and are already applied in user mode at the NSLS nanoprobe (HXN).

Additionally, detector development for X-ray fluorescence and X-ray diffraction has led to improvements of three orders of magnitude. Whereas in the past, measurements took seconds of dwell time per image pixel, scans are now feasible in the kHz range. The count rate capability was boosted by the introduction of SDD and multi-element detector arrays (*e.g.* Maia detector). Large detection solid angle, on-the-fly scanning mode and fast data acquisition and processing introduced the third dimension in scanning X-ray fluorescence microscopy, *i.e.* full 3D fluo-tomography and scanning spectro-microscopy. Pioneered at the Australian synchrotron XFM beamline [77], Maia is also operated at DESY P06 Microprobe [78], NSLS II, and CHESS. A setup from cryogenic X-ray fluorescence tomography with a Maia detector, cryo-stream (from above the sample capillary), and KB system (on the right) is shown in Fig. 9. Recent advances in digital signal processing electronics also allow scanning with millisecond dwell times with single or few-element SDD (APS 13-ID GSECARS, DLS I18).

4 Applications to environmental samples

4.1 Soil

Soil is a complex environmental matrix, heterogeneous down to the nanometre scale, where minerals, organic matter (large humic substances or smaller organic molecules), water, and air are intimately mixed, providing a suitable substrate for the growth and development of soil biota, including plants, fungi, and microorganisms.

Determining the amount, distribution, and speciation of trace elements in soils plays a pivotal role in assessing their availability to various organisms and their fate in the environment. When dealing with soil, a distinction has to be made between trace elements dissolved in the soil solution (mostly in a complexed form) and those present in the organic and inorganic solid phases. The analysis of dissolved trace elements mostly implies the use of methods derived from the field of aquatic chemistry. When it comes to X-ray analyses, liquid samples are not the most suitable for sensitive trace element detection, especially when using laboratory equipment like EDXRF and WDXRF. TXRF allows low detection limits for trace elements in liquid samples (down to ng g^{-1}), but only after complete evaporation of the solvent [79]. In this sense, TXRF analyses could be very useful in analysing trace elements in the soil solution, especially when only a few µl are extracted (*e.g.* through suction cups). For highly sensitive or speciation studies, however, synchrotron X-rays techniques are preferred. For quantification purposes, soil solutions or soil extracts (*e.g.* from selective extractions) can be analysed with SR XRF or TXRF. However, a more interesting application is trace element speciation by XAS. For this purpose, analysing frozen samples at very low temperatures (*i.e.* using liquid N_2 or He) is preferable, because of the better structural information attainable and the reduced radiation damage, which could either modify the oxidation state of the element or degrade the complexing molecule [80].

When dealing with trace elements in soil solid phases, X-ray based analytical methods most often give the best results compared to other analytical techniques, especially when spatially-resolved studies are needed. The total concentration of trace elements in soils can be directly quantified on solid samples by XRF or PIXE without the need of expensive and time-consuming preparation steps including digestion after drying and fine grinding. TXRF can also be used on digested soil samples after evaporation of the liquid phase. Soil powders can be analysed by XRD or XAS (as pressed pellets) for trace elements speciation in crystalline or/and amorphous solid phases, respectively. However, laboratory XRD instrumentation does not allow the detection of pure trace elements minerals, but instead detects major minerals containing trace elements in their lattice [81]. Spatially-resolved X-ray techniques are certainly among the most useful methods to study trace elements in soil, since they are able to resolve (at least partially) the great complexity of this environmental matrix. µ-XRF, SEM-EDX, and micro-PIXE are extremely valuable laboratory tools for microscopic soil analyses when the concentration of the element or the spatial resolution needed are in the range of 10 to 100 µg g^{-1} or 5 to 10 µm, respectively. For lower concentrations or higher spatial resolutions, synchrotron X-ray based techniques are needed [82]. These days, environmental beamlines usually permit combined analyses with spatially resolved XRF, XRD and XAS at resolutions from a few microns down to a few nanometres. Such techniques have been employed to identify solid phase species of (potential) contaminants in soils, assess the remediation of contaminated soils, study the transport of contaminants, evaluate fertiliser reactions in soils, investigate redox-sensitive elements, elucidate rhizosphere processes, and so on [9]. However, by also combining laboratory X-ray instruments (XRD, XRF, µ-XRF and SEM-EDX) with more "traditional" fractionation methods, like sequential extractions, assessments of trace element species and mobility in soil can be achieved, as reported by Allegretta *et al.* [83] for As in a former gold mining site (Fig. 10).

In a recent paper, Gattullo *et al.* [84] used a combination of all laboratory X-ray techniques (WD and ED XRF, XRD, µ-XRF, SEM-EDX, and XCMT) to evaluate the efficacy and the mechanisms of chromium(VI) remediation in a polluted soil, using glass and aluminium from municipal solid wastes as stabilising agents.

4.2 Rocks

Trace elements are studied in rocks for numerous reasons, usually related to a desire to understand geological and biogeochemical processes. Applications can range from research centered on mining for precious metals extraction to understanding major environmental and climatic changes over geological history. A number of reviews of the applications of X-ray techniques to understand trace elements in broad geological research and more specifically in rocks are available (*e.g.* [85]).

X-ray techniques, particularly XFM and microdiffraction, are uniquely situated to analyse trace elements in rocks alongside high concentration major elements, allowing quantitative elemental mapping on many

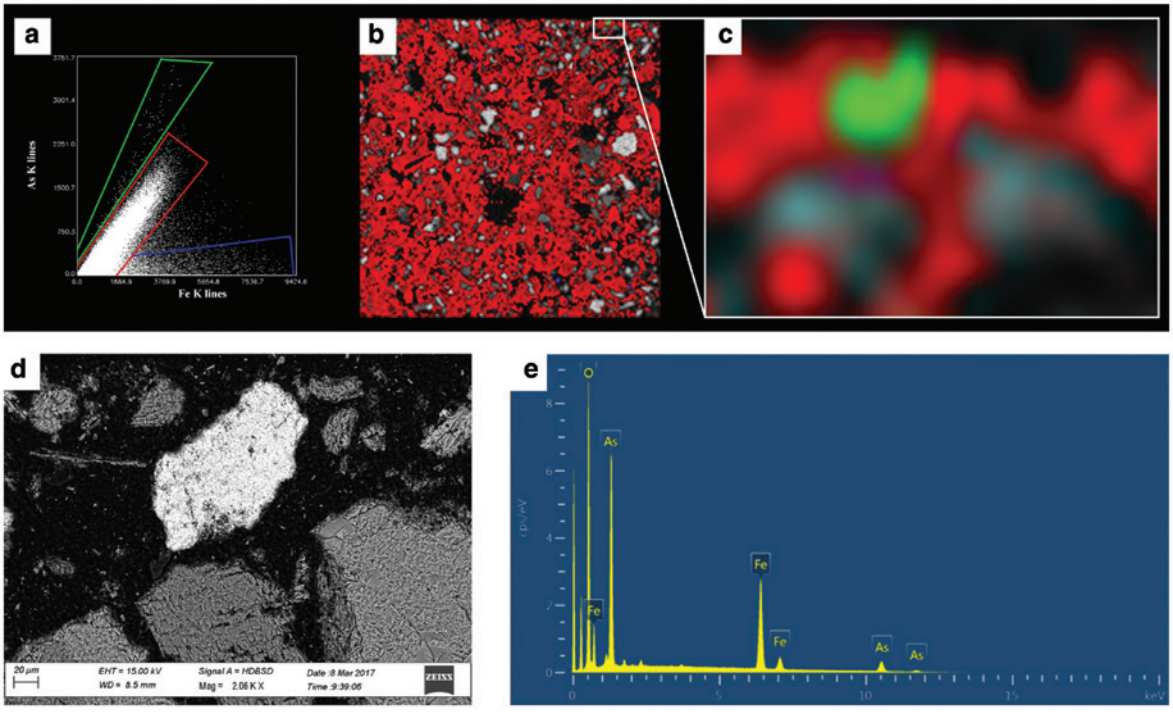

Fig. 10: μ-XRF (25 μm resolution) and FEG-SEM-EDX data of an As-polluted soil from the gold mining district of Monte Rosa (Italy). Maps were acquired on soil thin sections (32 μm thickness). μ-XRF spectra for each pixel of the map were elaborated and the arsenic and iron K-α fluorescence peak areas were plotted (a). Three different As/Fe ratios were identified (a) and imaged with green, red and blue colors on the Si K-α fluorescence map (grayscale) of soil thin sections (b). A magnification of the μ-XRF map showing a green domain corresponding to the highest As/Fe ratio (c). (d) Backscattered SEM micrograph of the area in (c). EDX analysis of the green particle in (c) showing the presence of Fe-arsenate (most probably scorodite) (e). Modified from [83].

length scales in order to understand, for example, the nature of mineral deposits. For this purpose, petrographic thin sections can be suitable objects to investigate, possibly using support glasses that do not contain the element(s) of interest.

Studies of ore systems require the microanalysis of samples to collect information on mineral chemistry in order to understand physiochemical conditions during ore genesis and alteration. Such studies contribute to the debate on whether precious metals are remobilised or introduced in multiple hydrothermal events [86].

Biogeochemical studies include research into beachrock formation *via* microbial dissolution and re-precipitation of carbonate minerals [87]. A wider environmental study looked at the release and transport of arsenic into aquifers of Bangladesh [88] to understand the geochemistry of processes that advance release and transport of As.

Besides elemental mapping and microdiffraction, understanding the oxidation state of trace elements in rocks is very important in geological and mineralogical studies. Examples include quantitative mapping of the oxidation state of iron in mantle garnet [89] and redox preconditioning in the deep cratonic lithosphere [90].

Chemical speciation mapping, or XANES imaging, is a powerful technique that has multiple applications in geology and rock research. One of the first demonstrations of XANES imaging was the study of arsenic speciation in an oxidised pisolitic regolith [64]. The same authors [64] also imaged an Fe-Mn metamorphosed ore sample, where arsenic(III) and arsenic(V) distribution was imaged by XANES on a thin section of 3.3 mm × 4 mm (Fig. 11). Chemical speciation mapping with XANES imaging has also been applied to many classes of environmental samples (*e.g.* [91]).

XFM can also be used to find very dilute and rare particles in geological systems and explore the uptake into plant systems [92]. In addition, in some cases depth resolved analyses can be done if there is sufficient detector diversity to enable analyses along various angular absorption paths [92].

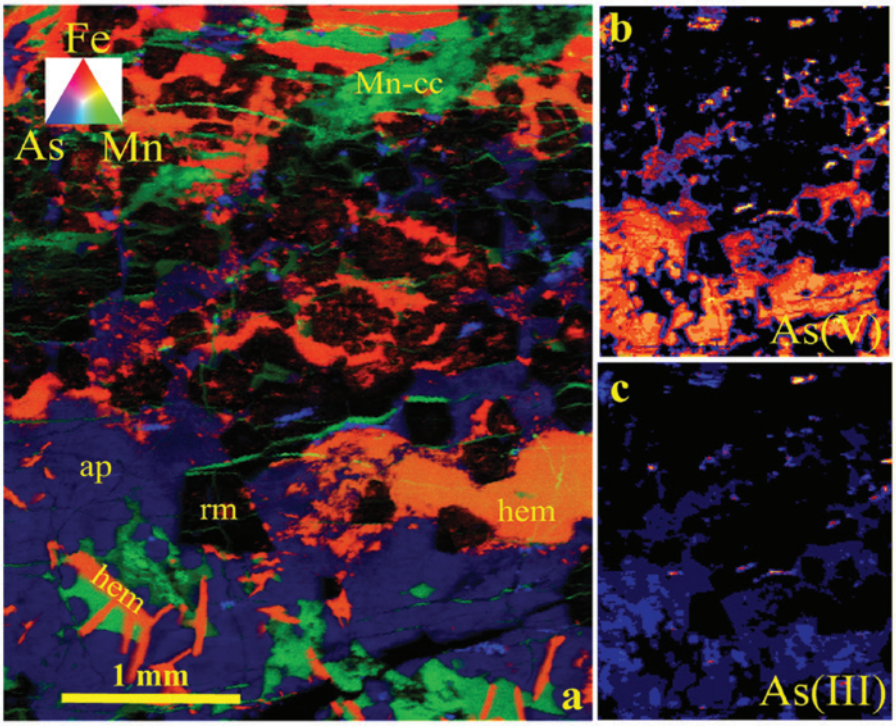

Fig. 11: Imaging of a Fe-Mn ore sample. (a) SXRF 2.112 million pixel RgB image built from the Fe, As, and Mn quantitative elemental maps (12.3892 keV; 3.3 × 4 mm²; 1.25 × 5 µm resolution; moving the sample stage with a velocity of 4.7 mm/s. (b and c) XANES images, smoothed with a boxcar filter over (20,4) pixels. Maximum concentrations (wt%): Fe = 65.7; As = 26.18; Mn = 29.8. ap = apatite, Mn-cc = Mn-calcite, hem = hematite, rm = roméite [64].

4.3 Waters and sediments

Across the world, trace elements are released in waters and sediments through normal geologic processes, *via* volcanic depositions, deep sea thermal vents, or geochemical weathering [93, 94]. Trace elements are also released into these environments as a result of anthropogenic activities *e.g.* mining discharges, the disposal/burning of consumer electronic waste, the application of fertilizers with micronutrients, and industrial releases *via* atmospheric deposition or solid waste discharges [95, 96]. Many inorganic elements, including Zr, Hf, Fe, Al, Th, Nb, and Sc, form compounds which are poorly soluble in water and therefore have limited mobility [93]. However, while these compounds may have limited solubility, they can be transported over long distances when sorbed to dissolved organic matter or micrometre- and nanometre-sized sediment particles that are easily suspended in waters [97]. The wind can carry these same dry sediments enriched in trace and rare earth elements (REE) from anthropogenic sources over long distances across terrestrial environments [98].

The use of synchrotron-based X-ray analyses has enhanced our knowledge of trace elements and REE in waters and sediments. Environmental chemists know that the physiochemical parameters controlling the partitioning of inorganic elements between waters and sediments include the pH, redox conditions, chemical speciation, particle size, organic matter, and the ligand exchange sites available for sorption [99].

Data collected from X-ray-based analyses is a tool that can be used to improve models and predictions. Confidence in models and the understanding of the fate and transport of trace elements in all media and environments is strongest when combining multiple independent analyses, which in turn yield congruent predictions [100]. For example, the combined use of micro-X-ray diffraction (µ-XRD) and micro-X-ray fluorescence (µ-XRF) mapping with EXAFS and XANES can identify the physical location, redox state, and nearest neighbours of trace elements in sediments or precipitation sites in bodies of water [94, 100]. These data can

then be used to improve the geochemical model's predictions of the fate and transport of trace elements in the environment, as well as new control technologies to prevent their release from industrial/mining activities.

A major advantage of XAS is the *in situ* analysis of trace elements to determine the redox state of the target analyte. However, researchers must be thoughtful and careful during the preparation of samples for XAS analyses. The photon beam itself can create artefacts. Sediments collected from flooded sites, lakes, or other bodies of water with oxic and anoxic conditions must be segregated and maintained in an environment equivalent to the redox state from which it was sampled for the whole duration of the analysis. Xu *et al.* [101] used XANES analyses to measure changes in As species and distribution in flooded sites from freeze-dried materials. The samples were processed in a glove box under a reduced atmospheric environment. To minimize changes in the redox state of a target analyte, it is a common practice in XAS analyses to freeze dried samples, analyse samples under vacuum or inert gases, and mount them with Kapton tape to prevent artefacts from being introduced in the laboratory [100]. Accurate speciation measurements of trace elements in the environment could be the difference between a costly remediation of a site, due to the presence of chromium(VI), or no action being taken at all, because chromium(III) is thermodynamically stable in oxidized environments [102].

Scientist, regulators, and stakeholders have focused attention on trace elements that demonstrate toxicity to humans and endanger ecosystem services such as clean drinking water and arable land. Arsenic, lead, and radioactive elements are among the most studied and dangerous trace elements monitored. Arsenic in drinking water should not exceed 10 μg L^{-1} [103], while the United States Environmental Protection Agency believes there is no safe level of lead in drinking water and therefore sets maximum contaminant level goal for lead at zero [104]. In areas of Southeast Asia, as well as North and South America, the groundwater has naturally occurring As concentrations that exceed 10 μg L^{-1} by multiple orders of magnitude and are responsible for many types of human cancers [105]. These same drinking waters in Southeast Asia are used for the irrigation of rice paddies. Performing μ-XRF and μ-XRD analyses, researchers showed that As from the groundwater was heterogeneously distributed within Fe hydroxide (oxides) in sediment aggregates and in the Fe-enriched rhizosphere of rice paddies [106]. The researchers also showed a mixture of reduced and oxidized As in the rhizosphere; however arsenic(V) was the predominate species present moving towards the oxygen enriched root surface. The implications of increased oxygen in the rhizosphere includes the decreased uptake of As into the rice plants and grains, as well as an increasing sorption of arsenic(V).

Researchers have shown that dissolved As in groundwater or in waters impacted from acid mine drainage are controlled in part by the redox state of the system, dissolved organic matter, and Fe minerals [107, 108]. In a novel experiment, Zhang *et al.* [109] provide insight into the sorption/desorption of As by Fe in an alluvial aquifer. The authors sorbed arsenic(III) and arsenic(V) to a variety of stable Fe minerals, as well as to the thermodynamically unstable Fe mineral ferrihydrite, and placed the minerals down in groundwater wells to monitor the changes in As and Fe minerals. Their research demonstrated that the partitioning of As sorbed to stable Fe minerals and dissolved into the groundwater was similar to past research findings but, additionally, using Fe-XANES the researchers observed the reductive dissolution of ferrihydrite and subsequent release of As into the groundwater.

Smedley and Kinniburgh [97] have written a review on Mo in natural waters (oceans, lakes, rivers). The molybdate anion is found at trace levels (μg L^{-1}) in oxic waters and oceans. In highly reducing euxinic environments, the concentration of Mo in waters can reach several hundred mg L^{-1}; Dahl *et al.* [110], using EXAFS and XANES, suggested that Mo in euxinic waters and sediments is controlled by Mo-Fe-S minerals with crystalline structures similar to nitrogenase enzymes. They hypothesized the Mo-Fe-S minerals would undergo reductive dissolution, releasing Mo into the pore water in the sediments or open water, possibly aided by the presence of dissolved organic matter.

The radioactive mutagenic element uranium has been released into the environment as a result of the mining and milling of U ores and the disposal of its waste products [111], as a result of aboveground nuclear testing, and *via* the use of depleted uranium (DU) ammunition [112], among other pathways. In a holistic study, Campbell *et al.* [111] combined XANES and EXAFS data with Mössbauer spectroscopy, traditional XRD

and XRF, liquid chemical extractions, and Phospholipid Fatty Acid (PLFA) and DNA analysis to monitor the biotic and abiotic cycling of U in lake sediments. Results from the XANES and EXAFS data suggested that the dominate U species present was uranium(IV). The minerals uraninite and coffinite, which feature U–U pairing at 3.85 Å, were not detected, although there was limited sampling due to trace levels of U in the sediments. The absences of the U–U pair suggest that there is little to no reductive cycling of U by metal-reducing bacteria, as demonstrated in laboratory batch experiments. However, the co-location of uranium(IV), iron(II), and reduced S phases suggested a complex sediment environment with large pool of reduced uranium(IV) and recalcitrant organic C, serving as electron donors for a microbial community that is reducing Fe and S minerals [114].

4.4 Plants

Plant research applied to environmental studies often aims at understanding how trace elements are acquired, transported, distributed, stored, and used in plants. This knowledge is important, not only for sustainable agricultural productions, but also for ensuring the nutritional quality and safety of agricultural products, as well as for plants used as bioindicators or in phytoremediation processes.

Trace element studies in plants usually aim at gaining the following information: concentration, localization, and chemical speciation. All of them are important to elucidate element homeostasis in plants. X-ray methods can provide all this information at the bulk scale, as well as at the tissue, cellular, and subcellular scales.

Less sensitive techniques, such as laboratory XRF, SEM-EDX, and PIXE, have been used to study hyperaccumulator and biofortified plants containing respectively high concentrations of toxic elements (*e.g.* Cd, As, Pb) or useful mineral nutrients (*e.g.* Fe, Zn, Se). Studying micronutrients or potentially toxic trace elements in non-hyperaccumulating plant species is much more challenging because of their low concentration. Obtaining the chemical speciation of trace elements presents an even greater challenge that can be overcome only by using synchrotron radiation techniques [113]. Recent overviews of the applications of synchrotron-based X-ray techniques to plants and soil-plant systems have been published by Sarret *et al.* [114] and Kopittke *et al.* [13] for elements such as Al, Cr, Mn, Co, Ni, Cu, Zn, As, Se, and Cd. Other relevant reviews on this issue are those by Donner *et al.* [115], Lombi *et al.* [116], Lombi and Susini [9], and Punshon *et al.* [117].

Sample preparation is one of the most critical steps involved in the X-ray analyses of plants, especially for spatially-resolved investigations and speciation studies. For total concentration analyses, sample drying and fine grinding are sufficient for good quantitative data using pressed pellets of “infinite” thickness [118]. For spatially-resolved analyses and speciation studies, sample preparation is often much more complex. In most cases, plant preparation consists in cryo-fixation by immersion in a cooled liquid or high-pressure freezing.

The simplest method is freeze-drying, which is useful for elemental localization studies at the tissue level but not at the cellular level, since element redistribution may be observed, as well as shrinkage of the cell structures. In addition, freeze-drying is not adapted for studies on metal speciation, since it may induce artefacts due to ion movement with water and structural modifications of aqueous complexes. To minimise perturbation, samples should remain in the hydrated frozen state. To achieve this, bulk samples are usually ground and homogenized in liquid nitrogen and then prepared as frozen pressed pellets to be analysed in a frozen state by means of instruments equipped with cryo-stages or cryo-chambers.

Because of the penetrating nature of X-rays, thin sections of uniform thickness should be prepared for 2D analyses, unless 3D investigations by means of confocal or tomographic techniques can be performed. Dried thin or ultrathin sections embedded in resin can be prepared after removing water. However, the elemental distribution and speciation can be altered by this preparation. Mature seeds contain low amounts of water and usually require minimal sample preparation compared to other plant organs [119]. Frozen hydrated samples can be prepared as thin sections by using a cryo-microtome and kept at low temperature until the

analysis. Cryo-preparations are usually less disturbing and limit the redistribution of metals and changes in speciation. Experiments can also be performed *in vivo*. However, in this case, exposure time under the beam should be reduced as much as possible and radiation damage should be monitored carefully. In general, the best preparation method depends on the technique available, the information that is required, and the nature of the plant material.

Indeed, sample damage is one of the most critical issues when biological samples like plants are analysed, especially when high energy particles or high X-ray fluxes (like at 3rd generation synchrotrons) are used.

Another important issue is related to the vacuum environments required by techniques like electron microscopy or PIXE and XRF (when light elements are to be investigated), which are detrimental to biological samples. In such cases, either cryo-stages can maintain water in frozen conditions, or special equipment like environmental-SEM (ESEM), which maintain a higher pressure at the sample while keeping the detector at a high vacuum, can be employed [120]. For these investigations, samples can also be analysed after either embedding or freeze-drying, as described above.

SEM and TEM-EDX systems provide nanometre-scale spatial resolution images of ultra-fine structure, but suffer high detection limits (about 100 μg g^{-1}), which usually restrict their use to the study of macronutrients or metal(loid)s in hyperaccumulator plants. Examples of such applications are found in Küpper *et al.* [121, 122] and Zhao *et al.* [123], who investigated the distribution of Zn in *Thlaspi caerulescens* and Cd and Zn in *Arabidospis halleri*. Other studies regarded the Ni hyperaccumulator *Alyssum lesbiacum* and *bertolonii* and *Thlaspi goesingense* [124], and the As hyperaccumulator *Pteris vittata* [125]. In a recent paper, Vigani *et al.* [126] imaged Zn distribution within single leaf cells of Fe-deficient cucumber (*Cuccumis sativus* L.) plants using an X-ray beam varying from 20 to 100 nm (Fig. 12).

PIXE can be used for bulk analysis of trace elemental concentrations [127, 128] or as a microprobe technique for elemental mapping. An extensive review of PIXE applications to plants is reported in Lombi *et al.* [12]. In general, PIXE offers good limits of detection (down to 1 mg kg^{-1}) on bulk samples and mapping of structures on the order of 10 to 100 μm.

TXRF analysis of bulk plant samples can extend the detection limits of XRF to ng g^{-1}. Samples can be analysed either as powder suspensions (a few μg mL^{-1}) or after acid digestion. Recently, the elemental composition of microgreens vegetables has been determined by Paradiso *et al.* [129] directly on powdered samples by TXRF. A very interesting potential application is the direct analysis of plant saps (*i.e.* xylem and phloem), because only a small amount of sample is required (a few μL).

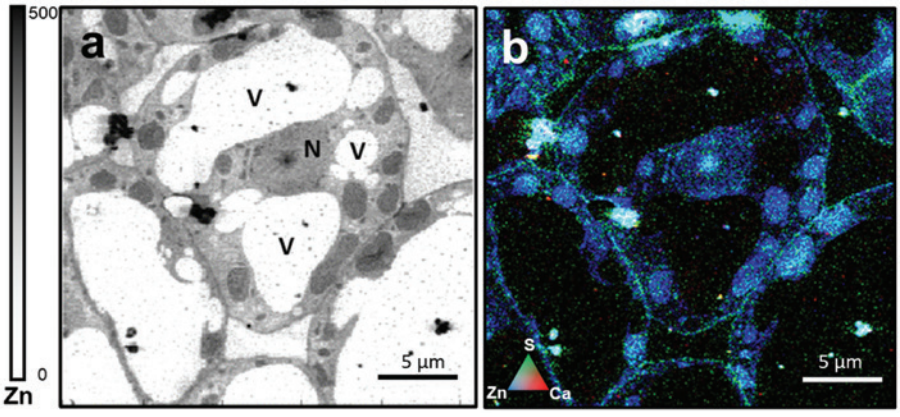

Fig. 12: (a) Subcellular zinc K-α X-ray fluorescence metal distribution map of a thin section (200 nm thickness) of a Fe-deficient cucumber leaf imaged by SRXM with 100 nm resolution. Darker pixels correspond to higher elemental concentrations. The scale bar reports the number of counts measured for Zn at each pixel of the image. An RGB image of the distribution of Zn (blue), S (green), and Ca (red) is also presented (b). N, nucleus; V, vacuole [126].

4.5 Other living organisms

XFM and XAS are uniquely situated to analyse trace elements in living organisms. Here we demonstrate the breadth of applications in environmental samples. The versatility of X-ray based techniques has allowed studies of living organisms across length scales ranging from single cells to whole animals. In many cases, the penetrating nature of X-rays allows analysis under environmentally relevant conditions and *in vivo* examinations.

Examples of studies in tissue and organ sections are: X-ray analysis to reveal asbestos fibres in human lungs [130], imaging the penetration and distribution of zinc and zinc species after topical application of zinc pyrithione to human skin [131], elemental homeostasis and the mechanisms of murine cerebral malaria to understand the altered cerebral metabolism, and protein oxidation at haemorrhage sites [132].

The versatility of trace element analysis has been demonstrated in a recent study that looked at trace element distribution in seabird feathers to understand the topobiology [133].

In vivo formation of natural HgSe nanoparticles in the liver and brain of pilot whales has been studied using XFM [134].

Whole animals can be studied using XFM, as with. for example, the direct *in vivo* imaging of essential bioinorganics in *Caenorhabditis elegans* [135] and the imaging of iron(II) dyshomeostasis in ageing *C. elegans* [136].

Laboratory μ-XRF [137] and TXRF [138] have been used to locate and quantify As accumulation in the coelomic fluids of earthworms (*Eisenia andrei*) grown on an As-polluted soil (Fig. 13).

The chemical speciation of trace elements in living organisms can be determined by using XAS and related methods. Living organism studies have been conducted *in vivo* where, for example, the oxidation state of metal-proteins has been determined using XANES imaging of coordination environments [70] and the high-resolution complementary chemical imaging of bio-elements in *C. elegans* [139].

Recent advances in fast and efficient XFM have allowed 3D information about spatial distribution of trace elements and their chemical speciation to be analysed at modern synchrotron facilities in realistic time scales, *e.g.* a few hours. Fluorescence X-ray absorption near-edge structure tomography has been used to study the spatial arrangement of biological coordination chemistry within intact organisms. This has been demonstrated by mapping the distribution of copper(I) and copper(II) complexes within *Drosophila melanogaster* [140].

Laboratory nanoparticle X-ray fluorescence tomography is an emerging imaging technique with potential for high-spatial-resolution molecular small-animal imaging [141]. Synchrotrons frequently use XRF for nanoparticle (NP) imaging, but the low-divergence beam and limited access to these facilities makes them less applicable for small-animal imaging [142].

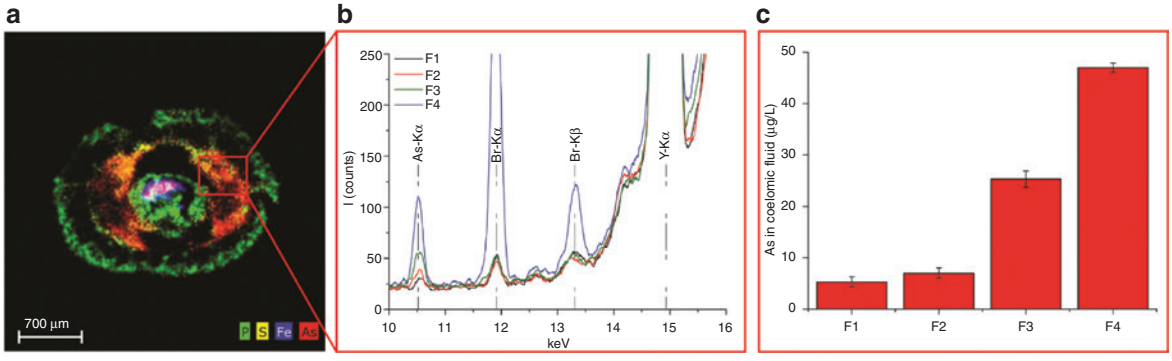

Fig. 13: μ-XRF distribution maps (25 μm resolution) of P, S, Fe and As in a thin section (200 μm thickness) of an earthworm exposed to an As-polluted soil (a). The As is mainly accumulated in the coelomic cavity. The coelomic fluids (F1, F2, F3 and F4) were extracted from four earthworms that lived in different soils containing 18, 21, 400 and 600 mg/kg of As, respectively. The coelomic fluids were extracted and analysed by TXRF (b). The As concentration in the coelomic fluids increased with the increase in the As contamination in soil (c). Modified from [137] and [138].

In a very recent publication by Cagno *et al.* [143], synchrotron radiation phase-contrast computed nanotomography and 2D and 3D nanoscopic XRF were used to investigate the internal distribution of engineered Co NPs in exposed individuals of the nematode *C. elegans* with 50 nm resolution.

4.6 Wastes

Trace elements in both solid and liquid wastes can be analysed by X-ray methods. However, element analyses of liquid matrices with X-rays often suffer from low signal-to-noise ratio (S/N) and therefore a range of different chemical and physical extraction techniques to overcome such problems have been developed. Most of these techniques aim at transferring the analytes into solid matrices, which then allows better results for trace elements analysis with X-rays ([144] and references therein).

X-ray based techniques can be used to determine trace element composition, distribution, and speciation in solid wastes. Solid wastes can have different characteristics (inorganic, organic, powders, pieces, crystalline, amorphous, *etc.*) and sizes (from nm to cm) and therefore sample preparation procedures cannot be generalized. However, for many waste samples, sample preparation is similar to that described for other solid matrices (*e.g.* soil, sediments, particulate, *etc.*).

Mining wastes have been studied using X-rays, with the aim of improving risk assessment, guiding appropriate mine planning for planned and active mines, and optimizing remediation design at closed or abandoned mines. In this field, the characterization of minerals is particularly important for predicting the potential for acidic drainage and metal(loid) leaching [145].

Another type of waste which has been extensively studied is that of biosolids derived from wastewater treatment systems, ranging from simple lagoon systems to activated sludge treatment plants with aerobic and anaerobic digestion. Such investigations are useful for the exploitation of contaminated/dirty biomass/biomass waste and potentially also as a tool in ascertaining the type/origin of biomass [146, 147].

Other types of wastes in which trace elements have been studied with X-rays are coal combustion by-products (*e.g.* bottom ash, fly ash), spoil wastes from marble quarries, red mud (from aluminium refineries), and construction and demolition wastes. All these materials can be studied at either the bulk scale or the microscopic scale, depending on the type of sample and information needed. For example, trace elements in coal fly ash particles have been investigated by TXRF [148] as suspensions to determine total concentration (*e.g.* to assess potentialities for recycling or disposal) or as single particles (*e.g.* to understand the processes of ash formation and trace elements segregation) [149].

A survey analysis and chemical characterization methodology for inhomogeneous solid waste samples (metals, alloys, salts, ores, plastics, organics) has been published by Sahlin and Magnusson [150] involving wavelength dispersive X-ray fluorescence with a fundamental parameters evaluation after homogenization and wax briquette preparation. Such a method is applicable to 49 elements and could be very useful in waste recycling and in the recovery of useful elements from wastes.

An interesting paper by Turner and Filella [151] reported the application of portable XRF to detect Br in plastic products as a proxy for the presence of bromine flame retardants (usually employed in electrical and electronic equipment), concluding that most of the plastic objects analysed were made from recycled electronic wastes, with a possible concern for consumers.

4.7 Nuclear wastes

The safe disposal of nuclear waste depends on the isolation of the waste from the geo- and bio-spheres. A worst-case scenario for disposed nuclear waste is the water-mediated leaching of radionuclides from the waste; these may then be mobilised and transported from the repository to the surrounding environment. Predicting, controlling, or prohibiting the transport of released radionuclides requires detailed knowledge of the physical and chemical determinant processes involved. Of central importance is the

radionuclide speciation, or its molecular, chemical, and physical form, as radionuclide speciation determines the balance of mobilization/immobilization processes, nuclide reactivity, and bioavailability; therefore, the radionuclide speciation defines potential human and environmental risk. Molecular-scale actinide speciation investigations using brilliant, focussed synchrotron sources are helping surmount experimental challenges related to nuclear waste disposal speciation studies, providing high sensitivity, elemental specificity and spatially-resolved information from chemical and physical heterogeneous matrices (*e.g.* waste forms, containers, back-fill materials, bedrock, spent fuels, *etc.*) [30, 152–154]. An example of μ-XRF and μ-XAS speciation investigation of neptunium in fractured granite follows, and is intended to demonstrate the utility of the techniques [155–157].

Following a tracer experiment investigating the transport of Np(V) using 0.01 mmol/dm^3 ^{237}Np eluted through a granite core from the Swedish Hard Rock Laboratory Äspö [158], a polished slice of the granite column containing most of the retained tracer activity (about 3 nmol Np/g; about 1 μg g^{-1}) was studied using a microfocussed X-ray beam in confocal geometry to identify the dominant neptunium immobilization process. Recorded scanning μ-XRF spectra allowed for the reconstruction of elemental distribution maps below the surface (Fig. 14a) by plotting the florescence intensity for selected elements as a function of sample position relative to the excitation source.

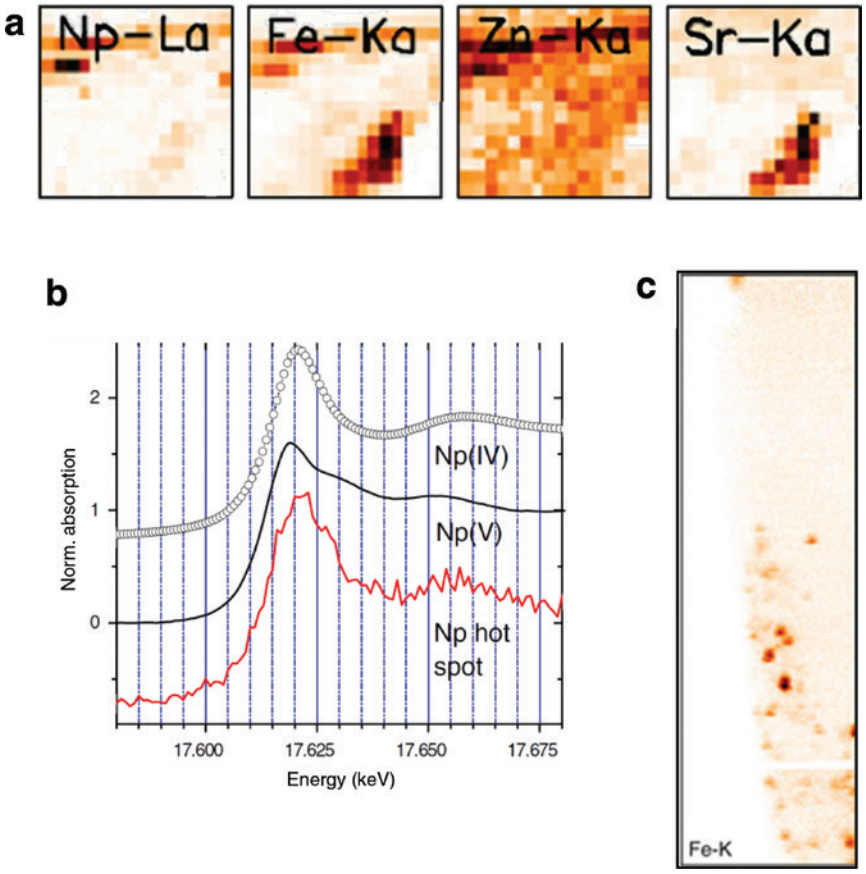

Fig. 14: (a) Elemental distribution maps for Np, Fe, Zn, and Sr in a 300 × 300 μm^2 section of a granite core slice (20 μm step size) reconstructed from μ-XRF data collected about 40 μm below the surface. (b) Np L3 XANES for neptunium(V) and neptunium(IV) references and μ-XANES measured at a Np hot spot –50 μm below the granite surface. Spectra are shifted on the y-axis for clarity. (c) Fe distribution in a 10.75 × 37.375 mm^2 (125 nm steps) area of a section of the granite cut out using focused ion beam (FIB). The exposed surface of a fissure evident in the lower half of the object exhibits nanoparticulate iron on the fissure wall. This area exhibited Np XRF intensity prior to FIBing, but no longer measureable Np fluorescence post FIBing.

Measuring in confocal geometry has three main advantages: minimizing sample preparation, avoiding potential artefacts from surface oxidation, and limiting the sample volume probed, which minimizes both background signal and spectral interference, in this particular case neptunium-L_α and strontium-K_α emission lines. An inspection of the elemental distributions in Fig. 10a reveals that the highest neptunium concentrations retained in the granite slice are in small, localised areas, indicated by clusters of pixels (or, because it is confocal, voxels) with high neptunium-L_α intensity. These areas are co-located with small granite fissures identified in the optical microscope images.

Neptunium-L_3 μ-XANES were recorded at neptunium hot spots below the surface; a representative spectrum is depicted in Fig. 14b and compared to reference spectra for neptunium(IV) and neptunium(V) species. The Np hot spots exhibit an ionisation energy and spectral features comparable to the neptunium(IV) reference, indicating that the Np originally introduced onto the granite column as a pentavalent species has been reduced to neptunium(IV). Note that without the spatial resolution it would have been impossible to obtain this information at such a dilute tracer concentration in a standard setup.

The observed concentration of Np into small areas associated with fissures can be interpreted as either formation of a precipitate or formation of sorbed species at localized areas on fissure walls. Spatially-resolved investigations with 125 nm resolution reveal that the Np is not sorbed onto fissure walls, however (Fig. 14c); the immobilised neptunium(IV) must be present as particulate (eigencolloid) species, most probably from hydrolysis of neptunium(IV). These low soluble particles simply become occluded in the small fissure spaces. The lower flow rates in small fissures, compared to larger fractures, allow longer residence (*i.e.* reaction) times for neptunium(V) reduction and immobilization to less soluble neptunium(IV). Additionally, a positive correlation was found between the Np distribution and that for Zn and to portions of areas with Fe (Fig. 14a). We may conclude that ZnS or Fe phases known to be in granite fissure material are likely reductants leading to neptunium(IV) formation, subsequent hydrolysis, and eigencolloid formation. These results have direct implications for modelling actinide retention for a nuclear repository in granite host rock. The redox potential of the groundwater/granite necessarily plays an important role, but realistic models must couple this to variations in hydrological transport affected by the size and interconnectivity of granite fractures and fissures.

4.8 Atmospheric particulate

Ambient particulate matter (PM) has long been recognized to have a detrimental effect on public health in urban areas. In particular, fine particles ($PM_{2.5}$) are more closely related to mortality and morbidity than coarse particles ($PM_{2.5–10}$), as these particles can penetrate deeply into the lungs. Ambient PM is a complex mixture consisting of a number of chemical constituents, such as carbonaceous, ionic, and elemental species. Characteristic elements, which are called “marker species”, have been employed to identify the source contribution to ambient aerosols. Once the characteristic elements are associated with a particular emission source, temporal resolved measurements can be made that provide detailed information about the emission characteristics of those sources.

The quantification of trace elements in airborne particulate matter (PM) can be achieved with various techniques, such as inductively coupled plasma mass spectrometry (ICP-MS), inductively coupled plasma optical emission spectrometry (ICP-OES), XRF, TXRF, PIXE, and EPMA. In contrast to the non-destructive XRF method, sample preparation for ICP analysis is laborious, and the samples are destroyed during this process. The measurement of low sample mass typically requires high sensitivity and hence access to a synchrotron facility. From high time resolutions down to those of one hour and less, impactors are used where the sample is collected on a foil or reflector. These samples are then exposed to X-rays without further treatment, which provides quantitative data with low detection limits down to the pg m^{-3} range. Access restrictions to synchrotrons limit the number of collected samples to be analysed, and hence field campaigns are predominantly episodic. Examples for elaborate studies of urban air are from Zürich [159–161] and London

[162, 163]. EPMA-automated atmospheric particle analysis has also been frequently employed, together with cluster analysis, to study atmospheric particulate composition and origin [164]. For this type of analysis, air sampling filters can be analysed directly without further treatment or just after being coated with a thin conductive carbon layer.

The SR-TXRF technique is often combined with XANES spectroscopy measurements. Osan *et al.* [165] collected aerosols at different urban locations in Hungary and revealed that the Cu and Zn speciation in the different size fraction was very distinctive for samples of different origin. Similar spectroscopy measurements were performed on the iron K-edge [166] to investigate the role of Fe in aerosols as oceanic micro nutrient, stimulating the growth of phytoplankton in the world seas. Light elements are the focus of studies of nitrogen and sulfur compounds in coastal Antarctic fine aerosol particles [167] and phosphorous determination in atmospheric aerosols [168]. Very recently, Shaltout *et al.* [169] studied size-fractionated aerosols collected from Jeddah, Saudi Arabia. A short review about aerosol characterization using synchrotron X-ray fluorescence is given by Fittschen [170].

Technical advances in X-ray sources and detectors have recently resulted in the development of commercial systems capable of sampling and analysing ambient PM samples in sub-hourly or hourly resolution in quasi-real time with an online XRF field analyser [171, 172] and are sufficient for standard applications. Instruments of this type can be used for continuous (months, years) monitoring at a site, but their cost may restrict the simultaneous deployment of a larger number of devices for different size fractions or at different sites.

5 Conclusions and perspectives

Improvements in the spatial resolution of X-ray based analytical techniques into the low nanometer range are ongoing. Improvements in emittance by orders of magnitude, due to the implementation of the multibend achromat technology, are expected at many synchrotrons in the coming years. Currently, beam sizes of 15 to 30 nm are routinely obtained at experiments like ESRF ID16A [173], APS 9-ID-B Bionanoprobe [76], and NSLS II Hard X-ray Nanoprobe. Extreme demagnification results in extreme flux density, which makes ultra-high vacuum and, especially for organic matter, cryogenic cooling, necessary in order to reduce carbon deposition and the impact of radiation damage. Along with optics development, instrumentation requires optimised stiffness and interferometric position control while maintaining the option of sample rotation for tomography. The high degree of coherence of current nanofocussed X-ray beams allows one to complement X-ray fluorescence microscopy with coherent X-ray imaging techniques like ptychography and X-ray phase contrast nanotomography in the same experiment. In this way, the trace element distribution is correlated with the structural image in highest resolution and allows functional correlation. Correlated ptychography with XFM is a major emerging technique that will become routine and make available super-resolution phase and absorption contrast information. Efforts are being made to integrate optical fluorescence microscopy and stimulated emission depletion (STED) microscopy as close as possible to the X-ray microscopy experiment.

The continuous improvement of X-ray techniques at synchrotron facilities and the growing awareness among environmental scientists of the tremendous potential of these methodologies have resulted in an increasing demand for experimental time at X-ray beamlines, making access highly competitive. However, recent developments in X-ray sources, optics, detectors, and sample stages (some of them previously developed for synchrotron applications), have made a number of commercial instruments available (especially in the field of XRF, XRD, and XCMT) with high analytical performances, which can complement or, in some cases, substitute for synchrotron applications. However, synchrotron applications remain unsurpassable when very low concentration trace elements (below 1 $\mu g\ g^{-1}$) and high spatial resolutions (below 1 μm) are to be studied, as is often the case for samples of environmental relevance.

Abbreviations

CRL	Compound Refractive Lenses
ED	Energy Dispersive
EPMA	Electron Probe Micro Analysis
ESEM	Environmental Scanning Electron Microscopy
EXAFS	Extended X-ray Absorption Fine Structure
FPGA	Field Programmable Gate Array
FZP	Fresnel-Zone Plates
ICP MS	Inductively Coupled Plasma Mass Spectrometry
ICP OES	Inductively Coupled Plasma Optical Emission Spectrometry
KB	Kirk-Patrick Baez
MLL	Multilayer Laue Lenses
PC	Poly Capillary
PIXE	Proton Induced X-ray Emission
PM	Particulate Matter
REE	Rare Earth Elements
SAXS	Small Angle X-ray Scattering
SDD	Silicon Drift Detector
SEM EDX	Scanning Electron Microscopy coupled to Energy Dispersive X-ray analysis
SR	Synchrotron Radiation
STED	Stimulated Emission Depletion
STXM	scanning transmission X-ray microscopy
TEM	Transmission Electron Microscopy
TXRF	Total Reflection X-ray Fluorescence
WD	Wavelength dispersive
XANES	X-ray Absorption Near Edge Structure
XAS	X-ray Absorption Spectroscopy
XCMT	X-ray computed microtomography
XFM	X-ray Fluorescence Microscopy
XFM CT	X-ray Fluorescence Micro-Computed Tomography
XRD	X-ray diffraction
XRF	X-ray fluorescence

Acknowledgements: This document was developed as a part of IUPAC, Funder Id: http://dx.doi.org/10.13039/100006987, Project #2016-019-2-600 "Trace elements analysis of environmental samples with X-rays: from synchrotron to lab and from lab to synchrotron" led by Roberto Terzano (Task Group Chair). Task Group Members for this project were: Melissa Anne Denecke, Gerald Falkenberg, Armin Gross, Koen Janssens, Bradley Miller, David Paterson, Ryan Tappero, Fang-Jie Zhao. Their contribution to the project is gratefully acknowledged.

Membership of the sponsoring body

Membership of the IUPAC Chemistry and the Environment Division Committee for the period 2016–2017 was as follows:

President: Dr. Petr Fedotov (Russia); **Past President:** Dr. Laura McConnell (USA); **Vice President:** Dr. Rai Kookana (Australia); **Secretary:** Prof. Hemda Garelick (UK); **Titular Members:** Dr. Manos Dassenakis (Greece); Dr. Philippe Garrigues (France); Dr. Irina Perminova (Russia); Dr. Heinz Rüdel (Germany); Dr. John B. Unsworth (UK); Dr. Baoshan Xing (USA); **Associate Members:** Prof. Guibin Jiang (China); Prof. Nadia G.

Kandile (Egypt); Prof. Gijs A. Kleter (Netherlands); Dr. Bradley W. Miller (USA); Prof. Stefka Tepavitcharova (Bulgaria); Prof. Roberto Terzano (Italy); **National Representatives:** Dr. Annemieke Farenhorst (Canada); Prof. Yong-Chien Ling (China/Taipei); Dr. Anna-Lea Rantalainen (Finland); Dr. Pradeep Kumar, FNA (India); Prof. Doo Soo Chung (Korea); Dr. Din Mohammad (Pakistan); Prof. Ana Aguiar-Ricardo (Portugal); Prof. Edgard Resto (Puerto Rico); Prof. Luke Chimuka (South Africa); Dr. Nelly Mañay (Uruguay).

For the period 2018–2019 was as follows: **President:** Prof. Rai Kookana (Australia); **Past President:** Prof. Petr S. Fedotov (Russia); **Vice President:** Prof. Hemda Garelick (UK); **Secretary:** Prof. Roberto Terzano (Italy); Titular Members: Prof. Doo Soo Chung (South Korea), Prof. Annemieke Farenhorst (Canada), Prof. Nadia G. Kandile (Egypt), Dr. Laura L. McConnell (USA), Prof. Irina Perminova (Russia), Prof. Fani L. Sakellariadou (Greece); **Associate Members:** Dr. Wenlin Chen (USA), Dr. Bradley Miller (USA), Prof. Diane Purchase (UK), Prof. Edgard Resto (Puesto Rico), Dr. John B. Unsworth (UK), Prof. Baoshan Xing (USA); **National Representatives:** Prof. Cristina Delerue Alvim de Matos (Portugal), Prof. Michal Galamboš (Slovakia), Prof. Ester Heath (Slovenia), Prof. Yong-Chien Ling (China/Tapei), Prof. Bulent Mertoglu (Turkey), Prof. Gloria Obuzor (Nigeria), Dr. Bipulbehari Saha (India), Dr. Tiina Sikanen (Finland), Prof. Weiguo Song (China), Prof. Stefka Tepavitcharova (Bulgaria).

References

[1] E. Liotti, A. Lui, T. Connolley, I. P. Dolbnya, K. J. S. Sawhney, A. Malandain, M. D. Wilson, M. C. Veale, P. Seller, P. S. Grant. *Sci. Rep.* **5**, 15988 (2015).
[2] K. D. Bradham, K. G. Scheckel, C. M. Nelson, P. E. Seales, G. E. Lee, M. F. Hughes. *Environ. Health Perspect.* **11**, 1629 (2011).
[3] K. D. Bradham, G. L. Diamond, K. G. Scheckel, M. F. Hughes, S. W. Casteel, B. W. Miller. *J. Toxicol. Environ. Health A*. **76**, 815 (2013).
[4] M. d. C. A. González-Chávez, B. W. Miller, I. E. Maldonado-Mendoza, K. G. Scheckel, R. Carrillo-González. *Fungal Biol.* **118**, 444 (2014).
[5] F. Porcaro, S. Roudeau, A. Carmon, R. Ortega. *TrAC, Trends Anal. Chem.* **104**, 22 (2018).
[6] P. W. Thrush. *A Dictionary of Mining, Mineral, and Related Terms*. U.S. Dept. of Interior, Bureau of Mines (1968).
[7] IUPAC. Compendium of Chemical Terminology (the "Gold Book"). Version 2.3.3, pp. 1551 (2014).
[8] G. E. Ice, J. D. Budai, J. W. L. Pang. *Science*. **334**, 1234 (2011).
[9] E. Lombi, J. Susini. *Plant Soil.* **320**, 1 (2009).
[10] M. Gräfe, E. Donner, R. N. Collins, E. Lombi. *Anal. Chim. Acta.* **822**, 1 (2014).
[11] G. M. Hettiarachchi, E. Donner, E. Doelsch. *J. Environ. Qual.* **46**, 1139 (2017).
[12] E. Lombi, K. G. Scheckel, I. M. Kempson. *Environ. Exp. Bot.* **72**, 3 (2011).
[13] P. M. Kopittke, P. Wang, E. Lombi, E. Donner. *J. Environ. Qual.* **46**, 1175 (2017).
[14] L. X. Chen. In *X-Ray Free Electron Lasers: Applications in Materials, Chemistry and Biology*, U. Bergmann, V. Yachandra (Eds.), pp. 201–224. Royal Society of Chemistry, London, UK (2017).
[15] G. Buzanich, M. Radtke, U. Reinholz, H. Riesemeier, A. F. Thünemanna, C. Strelib. *J. Anal. At. Spectrom.* **27**, 1875 (2012).
[16] J. Als-Nielsen, D. McMorrow. *Elements of Modern X-ray Physics*. Wiley-VCH, Germany (2011).
[17] R. Van Grieken, A. Markowicz. (Eds.). *Handbook of X-Ray Spectrometry*. Second Edition. Marcell Dekker, NY, USA (2002).
[18] J. A. Helsen, A. Kuczumov. In *Handbook of X-ray Spectrometry. Second Edition*, R. Van Grieken, A. A. Markowicz (Eds.), pp. 95–198. Marcell Dekker, NY, USA (2002).
[19] P. Kregsamer, C. Streli, P. Wobrauschek. In *Handbook of X-ray Spectrometry. Second Edition*, R. Van Grieken, A. A. Markowicz (Eds.), pp. 559–602. Marcell Dekker, NY, USA (2002).
[20] V. Scott, G. Love, S. Reed. *Quantitative Electron Probe Analysis*. Ellis Horwood, Boston, US (1995).
[21] S. Johansson, J. Campbell, K. Malmqvist. *Particle-Induced X-Ray Emission Spectrometry*. J. Wiley & Sons, Chichester, UK (1995).
[22] A. Rindby, K. Janssens. In *Handbook of X-ray Spectrometry. Second Edition*, R. Van Grieken, A. A. Markowicz (Eds.), pp. 631–718. Marcell Dekker, NY, USA (2002).
[23] K. Janssens, W. De Nolf, G. Van Der Snickt, L. Vincze, B. Vekemans, R. Terzano, F. E. Brenker. *TrAC* **29**, 464 (2010).
[24] A. A. Markowicz. In *Handbook of X-ray Spectrometry. Second Edition*, R. Van Grieken, A. A. Markowicz (Eds.), pp. 1–94. Marcell Dekker, NY, USA (2002).
[25] I. Szaloki, D. G. Lewis, C. A. Bennett, A. Kilic. *Phys. Med. Biol.* **44**, 1245 (1999).
[26] L. Vincze, K. Janssens, B. Vekemans, F. Adams. *Spectrochim. Acta Part B* **54**, 1711 (1999).
[27] W. Maenhaut, K. G. Malmqvist. In *Handbook of X-ray Spectrometry. Second Edition*, R. Van Grieken, A. A. Markowicz (Eds.), pp. 719–810. Marcell Dekker, NY, USA (2002).

[28] J. A. Small, D. E. Newbury. In *Handbook of X-ray Spectrometry. Second Edition*, R. Van Grieken, A. A. Markowicz (Eds.), pp. 811–932. Marcell Dekker, NY, USA (2002).
[29] J. A. Van Bokhoven, C. Lamberti. (Eds). *X-Ray Absorption and X-Ray Emission Spectroscopy: Theory and Applications*. John Wiley & Sons, Ltd, Chichester, UK (2016).
[30] M. A. Denecke. *Coord. Chem. Rev.* **250**, 730 (2006).
[31] Ph. Coppens. *X-Ray Charge Densities and Chemical Bonding*. Oxford University Press, UK (1997).
[32] F. Pfeiffer, T. Weitkamp, O. Bunk, C. David. *Nat. Phys*. **2**, 258 (2006).
[33] F. Döring, A. L. Robisch, C. Eberl, M. Osterhoff, A. Ruhlandt, T. Liese, F. Schlenkrich, S. Hoffmann, M. Bartels, T. Salditt, H. U. Krebs. *Opt. Express*. **21**, 19311 (2013).
[34] G. Chen, N. Bevins, J. Zambelli, Z. Qi. *Opt. Express*. **18**, 12960 (2010).
[35] O. Hemberg, M. Otendal, H. Hertz. *Appl. Phys. Lett.* **84**, 1482 (2003).
[36] N. Powers, I. Ghebregziabher, C. Golovin Liu, S. Chen, S. Banerjee, J. Zhang, D. Umstadter. *Nat. Photonics*. **8**, 29 (2014).
[37] H. Yumoto, H. Mimura, T. Koyama, S. Matsuyama, K. Tono, T. Togashi, Y. Inubushi, T. Sato, T. Tanaka, T. Kimura, H. Yokoyama, J. Kim, Y. Sano, Y. Hachisu, M. Yabashi, H. Ohashi, H. Ohmori, T. Ishikawa, K. Yamauchi. *Nat. Photonics*. **7**, 43 (2013).
[38] B. Lengeler, C. Schroer, M. Kuhlmann, B. Benner, T. Guenzler, O. Kurapova, F. Zontone, A. Snigirev, I. Snigireva. *J. Phys. D: Appl. Phys*. **38**, A218 (2005).
[39] K. Proost, L. Vincze, K. Janssens, N. Gao, E. Bulska, M. Schreiner, G. Falkenberg. *X-ray Spectrom*. **32**, 215 (2003).
[40] C. Chang, A. Sakdinawat. *Nat. Commun*. **5**, 4243 (2004).
[41] H. Kang, J. Maser, G. Stephenson, C. Liu, R. Conley, A. Macrander, S. Vogt. *Phys. Rev. Lett.* **96**, 127401 (2006).
[42] Z. Smit, K. Janssens, K. Proost, I. Langus. *Nucl. Instrum. Methods Phys. Res., Sect. B.* **219**, 35 (2003).
[43] L. Vincze, B. Vekemans, F. Brenker, G. Falkenberg, K. Rickers, A. Somogyi, M. Kersten, F. Adams. *Anal. Chem*. **76**, 6786 (2004).
[44] A. Woll, J. Mass, C. Bisulca, R. Huang, D. Bilderback, S. Gruner, N. Gao. Appl. Phys. A. **83**, 235 (2006).
[45] E. Gatti, P. Rehak. *Nucl. Instrum. Methods Phys. Res., Sect. A.* **541**, 47 (2005).
[46] R. Kirkham, P. Dunn, A. Kuczewski, P. Siddons, R. Dodanwela, G. Moorhead, C. Ryan, G. De Geronimo, R. Beuttenmuller, D. Pinelli, M. Pfeffer, P. Davey, M. Jensen, D. Paterson, M. de Jonge, D. Howard, M. Kusel, J. McKinlay. *AIP Conf. Proc*. **1234**, 240 (2010).
[47] I. Ordavo, S. Ihle, V. Arkadiev, O. Scharf, H. Soltau, A. Bjeoumikhov, G. Buzanich, R. Gubzhokov, A. Gunther, R. Hartmann, P. Holl, N. Kimmel, M. Kuhbacher, M. Lang, N. Langhoff, A. Liebel, M. Radkte, U. Reinholz, H. Riesemeier, G. Schaller, F. Schopper, L. Struder, C. Thamm, R. Wedell. *Nucl. Instrum. Methods Phys. Res., Sect. A.* **654**, 250 (2011).
[48] A. Mozzanica, A. Bergamaschi, S. Cartier, R. Dinapoli, D. Greiffenberg, I. Johnson, J, Jungmann, D. Maliakal, D. Mezza, C. Ruder, L. Schaedler, B. Schmitt, X. Shi, G. Tinti. *J. Instrum.* **9**, C05010 (2014).
[49] F. Romano, C. Caliri, L. Cosentino, S. Gammino, L. Giuntini, D. Mascali, L. Neri, L. Pappalardo, F. Rizzo, F. Taccetti. *Anal. Chem*. **86**, 10892 (2014).
[50] S. Vogt, A. Lanzirotti. *Synchrotron Radiation News*. **26**, 32 (2013).
[51] Y. Sun, S.-C. Gleber, C. Jacobsen, J. Kirz, S. Vogt. *Ultramicroscopy*. **152**, 44 (2015).
[52] A. Van der Ent, J. Wojciech, W. J. Przybyłowicz, M. D. de Jonge, H. H. Harris, C. G. Ryan, G. Tylko, D. J. Paterson, A. D. Barnabas, P. M. Kopittke, J. Mesjasz-Przybyłowicz. *New Phytol.* **218**: 432 (2018).
[53] R. Kirkham, P. A. Dunn, A. Kucziewski, D. P. Siddons, R. Dodanwela, G. F. Moorhead, C. G. Ryan, G. De Geronimo, R. Beuttenmuller, D. Pinelli, M. Pfeffer, P. Davey, M. Jensen, D. Paterson, M. D. de Jonge, M. Kusel, J. McKinlay. *AIP Conf. Proc*. **1234**, 240 (2010).
[54] D. P. Siddons, R. Kirkham, C. G. Ryan, G. De Geronimo, A. Dragone, A. J. Kuczewski, Z. Y. Li, G. A. Carini, D. Pinelli, R. Beuttenmuller, D. Elliott, M. Pfeffer, T. A. Tyson, G. F. Moorhead, P. A. Dunn. *J. Phys.: Conf. Ser.* **499**, 012001 (2014).
[55] C. G. Ryan, D. P. Siddons, R. Kirkham, Z. Y. Li, M. D. de Jonge, D. J. Paterson, A. Kuczewski, D. L. Howard, P. A. Dunn, G. Falkenberg, U. Boesenberg, G. De Geronimo, L. A. Fisher, A. Halfpenny, M. J. Lintern, E. Lombi, K. A. Dyl, M. Jensen, G. F. Moorhead, J. S. Cleverley, R. M. Hough, B. Godel, S. J. Barnes, S. A. James, K. M. Spiers, M. Alfeld, G. Wellenreuther, Z. Vukmanovic, S. Borg. *J. Phys.: Conf. Ser.* **499**, 012002 (2014).
[56] A. Levina, R. S. Armstrong, P. A. Lay. *Coord. Chem. Rev.* **249**, 141 (2005).
[57] T. Punshon, B. P. Jackson, A. Lanzirotti, W. A. Hopkins, P. M. Bertsch, J. Burger. *Spectrosc. Lett.* **38**, 343 (2005).
[58] G. N. George, I. J. Pickering, M. J. Pushie, K. Nienaber, M. J. Hackett, I. Ascone, B. Hedman, K. O. Hodgson, J. B. Aitken, A. Levina, C. Glover, P. A. Laye. *J. Synchrotron Radiat.* **19**, 875 (2012).
[59] I. J. Pickering, L. Gumaelius, H. H. Harris, R. C. Prince, G. Hirsch, J. A. Banks, D. E. Salt, G. N. George. *Environ. Sci. Technol.* **40**, 5010 (2006).
[60] D. H. McNear, R. L. Chaney, D. L. Sparks. *Phytochemistry*. **71**, 188 (2010).
[61] E. Montargès-Pelletier, V. Chardot, G. Echevarria, L. J. Michot, A. Bauer, J.-L. Morel. *Phytochemistry*. **69**, 1695 (2008).
[62] A. Van der Ent, L. Damien, D. L. Callahan, B. N. Noller, J. Mesjasz-Przybylowicz, W. J. Przybylowicz, A. Barnabas, H. H. Harris. *Scientific Reports*. **7**, 41861 (2017).
[63] R. Tappero. Microspectroscopic study of cobalt speciation and localization in hyperaccumulator *Alyssum murale*. 1–158 pp. PhD Thesis, University of Delaware, USA (2009).
[64] B. E. Etschmann, C. G. Ryan, J. Brugger, R. Kirkham, R. M. Hough, G. Moorhead, D. P. Siddons, G. De Geronimo, A. Kuczewski, P. Dunn, D. Paterson, M. D. de Jonge, D. L. Howard, P. Davey, M. Jensen. *Am. Mineral*. **95**, 884 (2010).

[65] H. A. Castillo-Michel, C. Larue, A. E. Pradas del Real, M. Cotte, G. Sarret. *Plant Physiol. Biochem*. **110**, 13 (2017).
[66] P. Wang, N. W. Menzies, E. Lombi, B. A. McKenna, S. James, S., C. Tang, P. M. Kopittke. *J. Exp. Bot.* **66**, 4795 (2015).
[67] J. Rothe, K. Dardenne, M. A. Denecke. *J. Colloid Interface Sci.* **231**, 91 (2000).
[68] I. J. Pickering, R. C. Prince, D. E. Salt, G. N. George. *Proc. Natl. Acad. Sci.* **97**, 10717 (2000).
[69] P. M. Kopittke, M. D. de Jonge, P. Wang, B. A. McKenna, E. Lombi, D. J. Paterson, D. L. Howard, S. A. James, K. M. Spiers, C. G. Ryan, A. A. T. Johnson, N. W. Menzies. *New Phytol.* **201**, 1251 (2014).
[70] S. A. James, D. J. Hare, N. L. Jenkins, M. D. de Jonge, A. I. Bush, G. McColl. *Scientific Reports* **6**, 20350 (2016).
[71] M. D. de Jonge, S. Vogt. *Curr. Opin. Struct. Biol.* **20**, 606 (2010).
[72] S. Mishra, M. Alfeld, R. Sobotka, E. Andresen, G. Falkenberg, H. Küpper. *J. Exp. Bot.* **67**, 4639 (2016).
[73] L. Vincze, B. Vekemans, F. E. Brenker, G. Falkenberg, K. Rickers, A. Somogyi, M. Kersten, F. Adams. *Anal. Chem*. **76**, 6786 (2004).
[74] E. Bulska, I. Wysocka, M. L. Wierzbicka, K. Proost, K. Janssens, G. Falkenberg. *Anal. Chem*. **78**, 7616 (2006).
[75] S. Mishra, G. Wellenreuther, J. Mattusch, H.-J. Staerk, H. Kuepper. *Plant Physiol*. **163**, 1396 (2013).
[76] S. Chen, J. Deng, Y. Yuan, C. Flachenecker, R. Mak, B. Hornberger, Q. Jin, D. Shu, B. Lai, J. Maser, C. Roehrig, T. Paunesku, S. C. Gleber, D. J. Vine, L. Finney, J. Vonosinski, M. Bolbat, I. Spink, Z. Chen, J. Steele. *J. Synchrotron Radiat.* **21**, 66 (2014).
[77] D. Paterson, M. D. de Jonge, D. L. Howard, W. Lewis, J. McKinlay, A. Starritt, M. Kusel, C. G. Ryan, R. Kirkham, G. Moorhead, D. P. Siddons. *AIP Conf. Proc*. **1365**, 219 (2011).
[78] U. Boesenberg, C. G. Ryan, R. Kirkham, D. P. Siddons, M. Alfeld, J. Garrevoet, T. Nunez, T. Claussen, T. Kracht, G. Falkenberg. *J. Synchrotron Radiat.* **23**, 1550 (2016).
[79] K. Vogel-Mikuš, P. Kump, M. Necemer, P. Pelicon, I. Arcon, P. Pongrac, B. Povh, M. Regvar. In *Soil Heavy Metals*, I. Sherameti, A. Varma (Eds.), pp. 113–138. Soil Biology Series, vol. 19, Springer-Verlag, Berlin-Heidelberg (2010).
[80] R. Terzano, T. Mimmo, B. Vekemans, L. Vincze, G. Falkenberg, N. Tomasi, M. Schnell Ramos, R. Pinton, S. Cesco. *Anal. Bioanal. Chem*. **405**, 5411 (2013).
[81] W. Harris, G. N. White. In *Methods of Soil Analysis, Part 5 – Mineralogical Methods*, A. L. Ulerey, L. R. Drees (Eds.), pp. 81–116. Soil Science Society of America, Madison, WI, USA (2008).
[82] A. Manceau, M. A. Marcus, N. Tamura. In *Rev. in Mineralogy and Geochemistry, vol 49: Applications of Synchrotron Radiation in Low-Temperature Geochemistry and Environmental Science*, P. Fenter, M. Rivers, N. C. Sturchio, S. Sutton (Eds.), pp. 341–428. Mineralogical Society of America, Washington, DC (2002).
[83] I. Allegretta, C. Porfido, M. Martin, E. Barberis, R. Terzano, M. Spagnuolo. *Environ. Sci. Pollut. Res*. **25**, 25080 (2018).
[84] C. E. Gattullo, C. D'Alessandro, I. Allegretta, C. Porfido, M. Spagnuolo. *J. Hazard. Mat.* **344**, 381 (2018).
[85] K. Tsuji, K. Nakano, Y. Takahashi, K. Hayashi, C.-U. Ro. *Anal. Chem.* **84**, 636 (2012).
[86] L. A. Fisher, D. Fougerouse, J. S. Cleverley, C. G. Ryan, S. Micklethwaite, A. Halfpenny, R. M. Hough, M. Gee, D. Paterson, D. L. Howard, K. Spiers. *Miner. Deposita.* **50**, 665 (2015).
[87] J. McCutcheon, J. L. D. Nothdurft, G. E. Webb, D. Paterson, G. Southam. *Mar. Geol.* **382**, 122 (2016).
[88] M. L. Polizzotto, C. F. Harvey, S. R. Sutton, S. Fendorf. *PNAS*. **102**, 18819 (2005).
[89] A. J. Berry, G. M. Yaxley, B. J. Hanger, A. B. Woodland, M. D. de Jonge, D. L. Howard, D. Paterson, V. S. Kamenetsky. *Geology.* **41**, 683 (2013).
[90] G. Yaxley, A. Berry, A. Rosenthal, A. Woodland, D. Paterson. *Scientific Reports*. **7**, 30 (2017).
[91] B. E. Etschmann, E. Donner, J. Brugger, D. L. Howard, M. D. de Jonge, D. Paterson, R. Naidu, K. G. Scheckel, C. G. Ryan, E. Lombi. *Environ. Chem.* **11**, 341 (2014).
[92] M. J. Lintern, C. G. Ryan, R. Anand, D. J. Paterson. *Nat. Comm.* **4**, 2614 (2013).
[93] J. J. Middelburg, C. H. van der Weijden, J. R. W. Woittiez. *Chem. Geol*. **68**, 253 (1988).
[94] R. Lafay, G. Montes-Hernandez, E. Janots, M. Munoz, A. L. Auzende, A. Gehin, R. Chiriac, O. Proux. *Geochim. Cosmochim. Acta*. **179**, 177 (2016).
[95] J. O. Nriagu, J. M. Pacyna. *Nature*. **333**, 134 (1988).
[96] J. M. Pacyna, E. G. Pacyna. *Environ. Rev.* **9**, 269 (2001).
[97] P. L. Smedley, D. G. Kinniburgh. *Appl. Geochem.* **84**, 387 (2017).
[98] R. S. Van Pelt, M. C. W. Barnes, J. E. Strack. *Aeolian Research*. **32**, 35 (2018).
[99] L.-C. Hsu, C.-Y. Huang, Y.-H. Chuang, H.-W. Chen, Y.-T. Chan, H. Y. Teah, T.-Y. Chen, C.-F. Chang, Y.-T. Liu, Y.-M. Tzou. *Scientific Reports*. **6**, 34250 (2016).
[100] S. Majumdar, J. R. Peralta-Videa, H. Castillo-Michel, J. Hong, C. M. Rico, J. L. Gardea-Torresdey. *Anal. Chim. Acta*. **755**, 1 (2012).
[101] L. Xu, X. Wu, S. Wang, Z. Yuan, F. Xiao, M. Yang, Y. Jia. *J. Hazard. Mater.* **301**, 538 (2016).
[102] D. G. Barceloux, D. Barceloux. J. *Toxicol. Clin. Toxicol.* **37**, 173 (1999).
[103] WHO. Guidelines for drinking-water quality: fourth edition incorporating the first addendum. Geneva, World Health Organization (2017).
[104] U.S. Environmental Protection Agency. National Primary Drinking Water Regulations for Lead and Copper: Short-Term Regulatory Revisions and Clarifications. 40 CFR 141 and 142. E. P. Agency. 2040–AE83 57782-57820 (2007).
[105] M. F. Naujokas, B. Anderson, H. Ahsan, H. V. Aposhian, J. H. Graziano, C. Thompson, W. A. Suk. *Environ Health Perspect.* **121**, 295 (2013).
[106] U. Kramar, S. Norra, Z. Berner, M. Kiczka, D. Chandrasekharam. *Appl. Geochem*. **77**, 4 (2017).

[107] P. Ravenscroft, H. Brammer, K. Richards. *Arsenic Pollution: A Global Synthesis*. Wiley, Chichester, UK (2009).
[108] H. Guo, C. Liu, H. Lu, R. B. Wanty, J. Wang, Y. Zhou. *Geochim. Cosmochim. Acta*. **112**, 130 (2013).
[109] D. Zhang, H. Guo, W. Xiu, P. Ni, H. Zheng, C. Wei. *J. Hazard. Mater.* **321**, 228 (2017).
[110] T. W. Dahl, A. Chappaz, J. P. Fitts, T. W. Lyons. *Geochim. Cosmochim. Acta*. **103**, 213 (2013).
[111] K. M. Campbell, R. K. Kukkadapu, N. P. Qafoku, A. D. Peacock, E. Lesher, K. H. Williams, J. R. Bargar, M. J. Wilkins, L. Figueroa, J. Ranville, J. A. Davis, P. E. Long. *Appl. Geochem*. **27**, 1499 (2012).
[112] Y. Wang, K. von Gunten, B. Bartova, N. Meisser, M. Astner, M. Burger, R. Bernier-Latmani. *Environ. Sci. Technol.* **50**, 12266 (2016).
[113] F. J. Zhao, K. L. Moore, E. Lombi, Y. G. Zhu. *Trends Plant Sci.* **19**, 183 (2014).
[114] G. Sarret, E. A. H. Smits, H. Castillo Michel, M. P. Isaure, R. Tappero. *Adv. Agron*. **119**, 1 (2013).
[115] E. Donner, T. Punshon, M. L. Guerinot, E. Lombi. *Anal. Bioanal. Chem.* **402**, 3287 (2012).
[116] E. Lombi, M. D. de Jonge, E. Donner, P. M. Kopittke, D. L. Howard, R. Kirkham, C. G. Ryan, D. Paterson. *PLoS ONE*. **6**, e20626–5 (2011b).
[117] T. Punshon, M. Guerinot, M. Lou, A. Lanzirotti. *Ann. Bot.* **103**, 665 (2009).
[118] J. L. de Vries, B. A. R. Vrebos. In *Handbook of X-Ray Spectrometry.* Second Edition. R. Van Grieken, A. Markowicz (Eds.), pp. 341–406. CRC Press, Boca Raton (2001).
[119] S. Astolfi, Y. Pii, R. Terzano, T. Mimmo, S. Celletti, I. Allegretta, D. Lafiandra, S. Cesco. *J. Cereal Sci.* **83**, 74 (2018).
[120] S. Sorbo, A. Basile, R. Castaldo Cobianchi. *Plant Biosyst.* **142**, 355 (2008).
[121] H. Küpper, F. J. Zhao, S. P. McGrath. *Plant. Physiol.* **119**, 305 (1999).
[122] H. Küpper, E. Lombi, F. J. Zhao, S. P. McGrath. *Planta.* **212**, 75 (2000).
[123] F. J. Zhao, E. Lombi, T. Brendon, S. P. McGrath. *Plant Cell Environ*. **23**, 507 (2000).
[124] H. Küpper, E. Lombi, G. Wieshammer, F. J. Zhao, S. P. McGrath. *J. Exp. Bot.* **52**, 2291 (2001).
[125] E. Lombi, F. J. Zhao, M. Fuhrmann, L. Q. Ma, S. P. McGrath. *New Phytol.* **156**, 195 (2002).
[126] G. Vigani, S. Bohic, F. Faoro, B. Vekemans, L. Vincze, R. Terzano. *Frontiers Plant Sci.* **9**, 1112 (2018).
[127] R. Giulian, C. E. I. dos Santos, S. D. M. Shubeita, L. M. da Silva, J. F. Dias, M. L. Yoneama. *J. Agr. Food Chem.* **55**, 741 (2007).
[128] M. C. Lagunas-Solar, C. P. U. C. Solis, A. Mireles. *Nucl. Instrum. Methods Phys. Res. B.* **266**, 2391 (2008).
[129] V. M. Paradiso, M. Castellino, M. Renna, C. E. Gattullo, M. Calasso, R. Terzano, I. Allegretta, B. Leoni, F. Caponio, P. Santamaria. *Food Funct.*, **9**, 5629 (2018)
[130] L. Pascolo, A. Gianoncelli, C. Rizzardi, M. de Jonge, D. Howard, D. Paterson, F. Cammisuli, M. Salomé, P. De Paoli, M. Melato, V. Canzonieri. *Microsc. Microanal.* **22**, 1062 (2016).
[131] A. Holmes, I. Kempson, T. Turnbull, D. Paterson, M. Roberts. *Toxicol. Appl. Pharmacol.* **343**, 40 (2018).
[132] M. J. Hackett, J. B. Aitken, F. El-Assaad, J. A. McQuillan, E. A. Carter, H. J. Ball, M. J. Tobin, D. Paterson, M. D. de Jonge, R. Siegele, D. D. Cohen, S. Vogt, G. E. Grau, N. H. Hunt, P. A. Lay. *Sci. Adv.* **1**, e1500911 (2015).
[133] N. Howell, J. L. Lavers, S. Uematsu, D. Paterson, D. L. Howard, K. Spiers, M. D. de Jonge, T. Hanley, R. Garrett, R. B. Banati. *Scientific Reports*. **7**, 1998 (2017).
[134] Z. Gajdosechova, M. M. Lawan, D. S. Urgast, A. Raab, K. G. Scheckel, E. Lombi, P. M. Kopittke, K. Loeschner, E. H. Larsen, G. Woods, A. Brownlow, F. L. Read, J. Feldmann, E. M. Krupp. *Scientific Reports.* **6**, 34361 (2016).
[135] S. A. James, M. D. de Jonge, D. L. Howard, A. I. Bush, D. Paterson, G. McColl. *Metallomics*. **5**, 627 (2013).
[136] S. A. James, b. R. Roberts, D. J. Hare, M. D. de Jonge, I. E. Birchall, N. L. Jenkins, R. A. Cherny, A. I. Bush, G. McColl. *Chem. Sci.* **6**, 2952 (2015).
[137] C. Porfido, I. Allegretta, O. Panzarino, R. Terzano, E. De Lillo, M. Spagnuolo. In: *Arsenic Research and Global Sustainability – Proceedings of the 6th International Congress on Arsenic in the Environment, AS 2016* (P. Bhattacharya, M. Vahter, J. Jarsjö, J. Kumpiene, A. Ahmad, C. Sparrenbom, G. Jacks, M. E. Donselaar, J. Bundschuh, R. Naidu (Eds.), pp. 341–343. CRC Press, The Netherlands (2016).
[138] I. Allegretta, C. Porfido, O. Panzarino, M. C. Fontanella, G. M. Beone, M. Spagnuolo, R. Terzano. *Spectrochim. Acta Part B* **130**, 21 (2017).
[139] D. J. Hare, M. W. M. Jones, V. C. Wimmer, N. L. Jenkins, M. D. de Jonge, A. I. Bush, G. McColl. *Metallomics.* **8**, 156 (2016).
[140] S. A. James, R. Burke, D. L. Howard, K. M. Spiers, D. J. Paterson, S. Murphy, G. Ramm, R. Kirkham, C. G. Ryan, M. D. de Jonge. *Chem. Commun.* **52**, 11834 (2016).
[141] N. Manohar, F. J. Reynoso, P. Diagaradjane, S. Krishnan, S. H. Cho. *Scientific Reports.* **6**, 22079 (2016).
[142] T. Paunesku, N. Stojicevic, S. Vogt, J. Maser, B. Lai, T. Rajh, M. Thurnauer, G. Woloschak. *J. Phys. IV.* **104**, 317 (2003).
[143] S. Cagno, D. A. Brede, G. Nuyts, F. Vanmeert, A. Pacureanu, R. Tucoulou, P. Cloetens, G. Falkenberg, K. Janssens, B., O. C. Lind. Anal. Chem. **89**, 11435 (2017).
[144] M. West, A. T. Ellis, P. J. Potts, C. Streli, C. Vanhoof, P. Wobrauschek. *J. Anal. At. Spectrom.* **31**, 1706 (2016).
[145] H. E. Jamieson, S. R. Walker, M. B. Parsons. *Appl. Geochem*. **57**, 85 (2015).
[146] E. Donner, D. L. Howard, M. D. De Jonge, D. Paterson, M. H. Cheah, R. Naidu, E. Lombi. *Environ. Sci. Technol.* **45**, 7249 (2011).
[147] E. Donner, K. Scheckel, R. Sekine, R. S. Popelka-Filcoff, J. W. Bennett, G. Brunetti, R. Naidu, S. P. McGrath, E. Lombi. *Environ. Pollut.* **205**, 78 (2015).
[148] A. K. Detcheva, S. E. Mitsiev, P. S. Vassileva, J. H. Jordanov, M. G. Karadjov, E. Ivanova. *Chem. Pap.* **69**, 650 (2015).

[149] L. Vincze, A. Somogyi, J. Osaán, B. Vekemans, S. Toöroök, K. Janssens, F. Adams. *Anal. Chem*. **74**, 1128 (2002).
[150] E. Sahlin, B. Magnusson. *Talanta*. **97**, 63 (2012).
[151] A. Turner, M. Filella. *Sci. Total Environ.* **584**, 982 (2017).
[152] M. A. Denecke. *J. Radioanal. Nucl. Chem*. **303**, 1339 (2015).
[153] M. A. Denecke. In *X-ray Absorption and X-ray Emission Spectroscopy: Theory and Application (Vol 1&2)*, J. A. van Bokhoven, C. Lamberti (Eds.), pp. 523–559. John Wiley and Sons, Chichester, UK (2016).
[154] T. Schäfer, M. A. Denecke. In: *X-Ray Optics and Microanalysis, Proceedings*, M. A. Denecke, C. T. Walker (Eds.), pp. 181–187, Amer. Inst. Physics Conference Proceedings, Melville, NY, USA, 1221 (2010).
[155] M. A. Denecke, K. Janssens, B. Brendebach, W. De Nolf, G. Falkenberg, J. Rothe, R. Simon, A. Somogyi, B. Vekemans, U. Noseck. In: *X-ray Absorption Fine Structure – XAFS13*, B. Hedman, P. Pianetta (Eds.), pp. 187–189. American Institute of Physics, Melville, NY (2007).
[156] M. A. Denecke, W. De Nolf, G. Falkenberg, K. Janssens, R. Simon. *Spectrochim. Acta, Part B.* **64**, 791 (2009).
[157] M. A. Denecke, W. de Nolf, A. Rack, R. Tucoulou, T. Vitova, G. Falkenberg, S. Abolhassani, P. Cloetens, B. Kienzler. In: *Actinide Nanoparticle Research*, S. N. Kalmykov, M. A. Denecke (Eds.), Springer Verlag, Heidelberg (2011).
[158] J. Römer, B. Kienzler, P. Vejmelka, E. Soballa, A. Görtzen, M. Fuß. FZK-wissenschaftliche berichte FZKA6770, Karlsruhe, Germany (2002).
[159] N. Bukowiecki, M. Hill, R. Gehrig, C. N. Zwicky, P. Lienemann, F. Hegedüs, G. Falkenberg, E. Weingartner, U. Baltensperger. *Environ. Sci. Technol.* **39**, 5754 (2005).
[160] A. Richard, N. Bukowiecki, P. Lienemann, M. Furger, M. Fierz, M. C. Minguillón, B. Weideli, R. Figi, U. Flechsig, K. Appel, A. S. H. Prévôt, U. Baltensperger. *Atmos. Meas. Tech.* **3**, 1473 (2010).
[161] A. Richard, M. F. D. Gianini, C. Mohr, M. Furger, N. Bukowiecki, M. C. Minguillón, P. Lienemann, U. Flechsig, K. Appel, P. F. DeCarlo, M. F. Heringa, R. Chirico, U. Baltensperger, A. S. H. Prévôt. *Atmos. Chem. Phys.* **11**, 8945 (2011).
[162] S. Visser, J. G. Slowik, M. Furger, P. Zotter, N. Bukowiecki, R. Dressler, U. Flechsig, K. Appel, D. C. Green, A. H. Tremper, D. E. Young, P. I. Williams, J. D. Allan, S. C. Herndon, L. R. Williams, C. Mohr, L. Xu, N. L. Ng, A. Detournay, J. F. Barlow, C. H. Halios, Z. L. Fleming, U. Baltensperger, A. S. H. Prévôt. *Atmos. Chem. Phys.* **15**, 2367 (2015).
[163] S. Visser, J. G. Slowik, M. Furger, P. Zotter, N. Bukowiecki, F. Canonaco, U. Flechsig, K. Appel, D. C. Green, A. H. Tremper, D. E. Young, P. I. Williams, J. D. Allan, H. Coe, L. R. Williams, C. Mohr, L. Xu, N. L. Ng, E. Nemitz, J. F. Barlow, C. H. Halios, Z. L. Fleming, U. Baltensperger, A. S. H. Prévôt. *Atmos. Chem. Phys.* **15**, 11291 (2015).
[164] S. Hoornaert, R. H. M. Godoi, R. Van Grieken. *Chem.* **48**, 301 (2004).
[165] J. Osán, F. Meirer, V. Groma, S. Török, D. Ingerle, C. Streli, G. Pepponi. *Spectrochim. Acta, Part B.* **65**, 1008 (2010).
[166] U. E. A. Fittschen, F. Meirer, C. Streli, P. Wobrauschek, J. Thiele, G. Falkenberg, G. Pepponi. *Spectrochim. Acta, Part B.* **63**, 1489 (2008).
[167] J. Osán, S. Török, B. Beckhoff, G. Ulm, H. Hwang, C.-U. Ro, C. Abete, R. Fuoco. *Atmos. Environ.* **40**, 4691 (2006).
[168] U. E. A. Fittschen, C. Streli, F. Meirer, M. Alfeld. *X-Ray Spectrom.* **42**, 368 (2013).
[169] A. A. Shaltout, M. Harfouche, S. I. Ahmed, M. Czyzycki, A. G. Karydas. *Microchem. J.* **137**, 78 (2018).
[170] U. E. A. Fittschen. *Spectrosc. Eur*. **26**, 10 (2014).
[171] M. Furger, M. C. Minguillón, V. Yadav, J. G. Slowik, C. Hüglin, R. Fröhlich, K. Petterson, U. Baltensperger, A. S. H. Prévôt. *Atmos. Meas. Tech.*, **10**, 2061 (2017).
[172] S.-S. Park, S. Y. Cho, M. R. Jo, B. J. Gong, J. S. Park, S. J. Lee. *Atmos. Pollut. Res.* **5**, 119 (2014).
[173] C. Sanchez-Cano, I. Romero-Canelón, Y. Yang, I. J. Hands-Portman, S. Bohic, P. Cloetens, P. J. Sadler. *Chem. – Eur. J.* **23**, 2512 (2017).